ACS APPLIED NANO MATERIALS

www.acsanm.org
Article

Dissipative Particle Dynamics Models of Encapsulated Microbubbles and Nanoscale Gas Vesicles for Biomedical Ultrasound Simulations

Nikolaos Ntarakas, Maša Lah, Daniel Svenšek, Tilen Potisk, and Matej Praprotnik*

Cite This: ACS Appl. Nano Mater. 2025, 8, 16053−16070
Read Online

ABSTRACT: Ultrasound-guided drug and gene delivery (USDG) enables controlled and spatially precise delivery of drugs and macromolecules, encapsulated in microbubbles (EMBs) and nanoscale gas vesicles (GVs), to target areas such as cancer tumors. It is a noninvasive, high precision, low toxicity process with drastically reduced drug dosage. Rheological and acoustic properties of GVs and EMBs critically affect the outcome of USDG and imaging. Detailed understanding and modeling of their physical properties is thus essential for ultrasound-mediated therapeutic applications. State-of-the-art continuum models of shelled bodies cannot incorporate critical details such as varying thickness of the encapsulating shell or specific interactions between its constituents and interior or exterior solvents. Such modeling approaches also do not allow for detailed modeling of chemical surface functionalizations, which are crucial for tuning the GV−blood interactions. We develop a general particle-based modeling framework for encapsulated bodies that accurately captures elastic and rheological properties of GVs and EMBs at the mesoscopic and nanoscale levels. We use dissipative particle dynamics to model the solvent, the gaseous phase in the capsid, and the triangulated surfaces of immersed objects. Their elastic behavior is studied and validated through stretching and buckling simulations, eigenmode analysis, shear flow simulations, and comparison of predicted GV buckling pressure with published experimental data. The presented modeling approach paves the way for large-scale simulations of nanoscale and microscale encapsulated bodies of different shapes and local anisotropy, capturing their dynamics, interactions, and collective behavior.

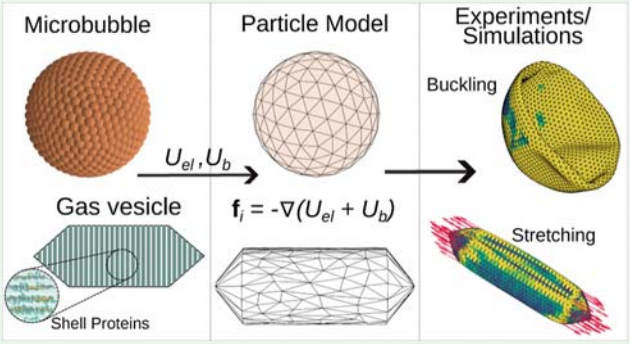

KEYWORDS: *ultrasound, gas vesicles, proteinaceous nanostructures, microbubbles, particle simulations, mesoscopic modeling*

1. INTRODUCTION

Ultrasound (US) is increasingly being used in biomedical applications to diagnose many types of cancer, for blood flow analysis and therapeutic applications, including thermal tissue coagulation, kidney stones fragmentation, bone healing, mechanical tissue disruption and in cases of joint inflammation or rheumatoid arthritis.[1−7] It offers numerous advantages, such as functionality in opaque media, relatively high spatial precision on the micrometer scale and fast, reconfigurable field formation.[8] These features have made US a cornerstone of modern biomedical imaging and therapy.

To further enhance the capabilities of US in diagnostics and therapeutics, a diverse set of responsive agents has been developed, including encapsulated biomaterials and even synthetic nano- and microrobots.[9,10] Encapsulated biomaterials[2,11] have emerged as powerful tools due to their unique design and shell properties make them highly adaptable for two major US biomedical applications: enhancing US imaging as ultrasound contrast agents (UCAs)[1,5,11,12] and enabling the encapsulation and targeted delivery of therapeutic drugs.[1,2,11−18] Among these materials, encapsulated microbubbles (EMBs) and gas vesicles (GVs) have garnered significant attention for their adaptability and effectiveness in such applications. Radial oscillations of EMBs and GVs generate strong nonlinear acoustic signals with a unique signature in the acoustic field and a frequency range much greater than that produced by tissues. This allows them to generate significant US contrast across a range of frequencies, supporting harmonic, multiplexed, and multimodal US imaging, as well as cell-specific molecular targeting.[19,20]

EMBs injected into the bloodstream are already being used for echocardiography,[11,13,21] which is one of the essential tools for diagnosing cardiovascular diseases. EMBs are typically 1 μm in diameter and consist of biologically inert gases, such as air or gases with lower water solubility, stabilized within a lipid,

Received: June 5, 2025
Revised: July 25, 2025
Accepted: July 28, 2025
Published: August 4, 2025

https://doi.org/10.1021/acsanm.5c02783
ACS Appl. Nano Mater. 2025, 8, 16053−16070

protein, or polymer shell.[1,12,22] When an EMB is subjected to a high-intensity acoustic field, it expands in volume and collapses violently. This process is known as inertial cavitation.[23] In contrast, during noninertial or stable cavitation, EMBs oscillate with relatively minor deformations under lower acoustic pressure amplitudes. Cavitation is utilized in sonoporation,[24] which is a targeted drug delivery technique that creates temporary pores in cell membranes, enabling the entry of foreign substances.[14,25] Exploiting the sonoporation effect for disease therapy has many advantages, for instance, injecting EMBs intravenously can lower drug dosage and minimize side effects of nonspecific drug delivery into healthy organs as the EMBs only collapse in specific diseased areas due to focused US irradiation. One limitation to the use of EMBs is their size, which prevents them from extravasating into tumors. To circumvent this limitation, GVs have been introduced as a new class of nanoscale US imaging agents.[26−32]

GVs are gas-filled, protein-shelled nanostructures produced by buoyant photosynthetic microbes. These vesicles vary in size, with widths ranging from 45 to 200 nm and lengths from 100 to 800 nm, depending on their genetic origin, and can withstand external pressures of several bar without collapsing. Recently, GVs have also been shown to increase the influx of calcium ions, when attached to biological cells and insonated by US.[33] The structure of several types of GVs has already been characterized using cryo-EM (Cryogenic electron microscopy) and cryo-ET (Cryogenic electron tomography),[34,35] revealing that the main structural protein GvpA self-assembles helically in a cylindrical shape, which closes off on both sides by cone-shaped tips. The polarity of the helical assembly inverts at the midpoint of the GV cylinder, which may act as an elongation center for growth. This implies that the ribs are oriented helically along the cylinder, reversing direction at the central rib.[34,36] Unlike EMBs, which confine preloaded gas in an unstable state, GVs have 2 nm-thick protein shells that exclude water but allow gas to diffuse in and out of their interior.[37]

The acoustic behavior of EMBs and GVs is influenced by several factors, such as the viscosity and temperature of the surrounding fluid, the applied acoustic pressure and the physical characteristics of the objects, including size and shell properties like viscosity and elasticity.[38,39] In addition, the presence of nearby vessel walls or cells can significantly affect the EMB behavior.[39] Unlike the detailed modeling of blood flow[40−55] or cloud cavitation collapse,[56,57] the current theoretical modeling of EMB oscillations primarily relies on the continuum theory developed by Rayleigh and Plesset for a single, free, spherically symmetric bubble in an infinite liquid with constant viscosity.[58,59] The Rayleigh-Plesset EMB model incorporates several assumptions, including the ideal gas behavior of the encapsulated gas and the absence of a shell. A series of increasingly complex models have been developed to more accurately represent the dynamics of EMBs in vivo—particularly those excited by US while flowing through small blood vessels. Despite these improvements, the models continue to rely on various assumptions and simplifications.[60−62] A novel stress−strain method[63] was derived to characterize the viscoelastic shells of individual lipid-shelled US-driven microbubbles, aiming to extract their elastic and viscous properties with minimal assumptions.

Continuum models for GVs are very scarce, with the exception of finite element models for various types of GVs, such as the Anabaena flos-aquae[20,34,64,65] and the *Halobacterium salinarum*,[66] which focus purely on mechanical properties in vacuum, without explicitly modeling the surrounding solvent or encapsulated gas. A microscopic model has been reported,[67] in which a model for the GvpA rib was developed and used to calculate the Young's moduli of the GV shell. A recent paper[68] examined the use of GVs as cavitation nuclei, where the authors conducted simulations of bubbles formed by the coalescence of gas released from destroyed GVs. Although significant efforts have been made to improve continuum models for EMBs and GVs,[38,60,62,66,69−77] accurately modeling the shell properties before and after insonation remains a challenging task. The applicability of continuum models in these scenarios is limited, mainly due to the lack of detailed interfacial constitutive models.[60] These limitations of existing continuum models preclude an accurate description of cavitation, drastically degrading the prediction of drug delivery outcomes.

The development of novel EMBs and GVs models using mesoscopic particle-based approaches tailored to the specific shell material is crucial to study changes in the material upon deformation and its mechanical response to interaction with US. Importantly, the mechanical behavior of UCAs differs significantly between water and blood, due to variations in viscosity, elasticity, and the complex interplay with surrounding EMBs and vesicles in the bloodstream. Incorporating these factors into simulations is essential for accurate predictions of their performance in real physiological environments. To accurately capture the rheological and acoustic properties, as well as the dynamics of EMBs and GVs, we propose mesoscopic particle-based models inspired by the network models of red blood cells (RBCs). The proposed models are designed to be general enough to accommodate a wide range of physical systems. Here, we use the dissipative particle dynamics (DPD) method, a state-of-the-art particle-based method for modeling colloidal suspensions, polymers, soft matter, and simple fluids. We model mechanical properties of EMBs and GVs, including their behavior in stretching and buckling experiments. Our predictions for the buckling pressure of GVs are compared to experimental measurements. Furthermore, we determine fundamental eigenmodes of EMBs and GVs. Finally, we study their rheological properties under shear flow and compare them with analytical expressions.

2. METHODS

The simulations were carried out using Mirheo,[78] a high-throughput simulation package, specifically designed and optimized for DPD simulations. While isotropic elastic forces are already implemented in Mirheo, we modified and extended its functionalities to include orthotropic elastic forces, the gas pressure contribution as well as the OBMD used in nonequilibrium simulations.

2.1. Dissipative Particle Dynamics. The DPD method[79] is a particle-based mesoscopic simulation technique that allows modeling of fluids and soft matter.[80,81] A DPD system is represented by N particles, which interact through pairwise effective potentials and move according to Newton's second law. In a DPD simulation, a particle represents a cluster of molecules. In our case, the DPD particle represents a large number of water or gas molecules.

The interparticle force $\mathbf{F}_{ij} = \mathbf{F}_{ij}^C + \mathbf{F}_{ij}^D + \mathbf{F}_{ij}^R$ exerted by bead j on bead i consists of conservative, dissipative, and random forces[82]

$$\mathbf{F}_{ij}^{\mathrm{C}} = a_{\alpha\beta}\omega_{\mathrm{C}}(r_{ij})\hat{\mathbf{r}}_{ij} \tag{1}$$

$$\mathbf{F}_{ij}^{\mathrm{D}} = -\gamma_{\alpha\beta}\omega_{\mathrm{D}}(r_{ij})(\mathbf{v}_{ij}\cdot\hat{\mathbf{r}}_{ij})\hat{\mathbf{r}}_{ij} \tag{2}$$

$$\mathbf{F}_{ij}^{\mathrm{R}} = \sigma_{\alpha\beta}\omega_{\mathrm{R}}(r_{ij})\Theta_{ij}\hat{\mathbf{r}}_{ij} \tag{3}$$

https://doi.org/10.1021/acsanm.5c02783
ACS Appl. Nano Mater. 2025, 8, 16053−16070

where $a_{\alpha\beta}$ and $\gamma_{\alpha\beta}$ represent the conservative and dissipative parameters for a bead pair of species α and β (water, gas, UCA object), specified in Table 1, $\sigma_{\alpha\beta}$ is the random force amplitude

Table 1. Values of the DPD Parameters Used, Unless Stated Otherwise, for EMB and GV Unit Sets[a]

DPD parameter	value (EMB unit set)	value (GV unit set)
a_{ww}	$100.0\,\frac{k_BT_0}{r_c}$	$100.0\,\frac{k_BT_0}{r_c}$
a_{wg}, a_{gg}, a_{oo}, a_{og}	$0.0\,\frac{k_BT_0}{r_c}$	$0.0\,\frac{k_BT_0}{r_c}$
a_{ow}	$40\,\frac{k_BT_0}{r_c}$	$40\,\frac{k_BT_0}{r_c}$
γ_{ww}	$3.5\,\frac{m}{\tau}$	$18.0\,\frac{m}{\tau}$
γ_{gg}	$11.0\,\frac{m}{\tau}$	$12.0\,\frac{m}{\tau}$
γ_{wg}	$0.0\,\frac{m}{\tau}$	$0.0\,\frac{m}{\tau}$
γ_{ow}	$7.4\,\frac{m}{\tau}$	$19.5\,\frac{m}{\tau}$
γ_{og}	$0.2\,\frac{m}{\tau}$	$0.5\,\frac{m}{\tau}$
ρ_w, ρ_g	$3.0\,r_c^{-3}$	$3.0\,r_c^{-3}$
k_{ww}	0.25	0.125
k_{gg}	0.25	0.0
k_{fsi}	0.5	0.5

[a]The subscripts denote the different types of beads: (o)bject, (w)ater, (g)as.

connected with the dissipative parameter $\gamma_{\alpha\beta}$ (S4.1), $\hat{\mathbf{r}}_{ij} = \frac{\mathbf{r}_i - \mathbf{r}_j}{|\mathbf{r}_i - \mathbf{r}_j|}$ is the normalized vector along the interparticle axis, $\mathbf{v}_{ij} = \mathbf{v}_i - \mathbf{v}_j$ the relative velocity of the two interacting particles, ω_C, ω_D, ω_R are the weight kernels described in S4.1, while $\Theta_{ij} = \Theta_{ji}$ is a zero-mean random Gaussian variable with unit variance, uncorrelated between different pairs of particles i and j

$$\langle \Theta_{ij}(t)\Theta_{kl}(t')\rangle = (\delta_{ik}\delta_{jl} + \delta_{jk}\delta_{il})\delta(t - t') \tag{4}$$

The equation of state of a DPD fluid is quadratic in the density

$$p = \rho k_B T_0 + \alpha a_{ww}\rho^2 \tag{5}$$

where $\alpha \approx 0.100 r_c^4$ is a semiempirical prefactor.[83]

2.2. Membrane Modeling. We represent the GV and EMB membranes as triangulated surfaces, where each vertex corresponds to a DPD bead (particle). Interactions between these membrane particles are derived from a discretized continuum elastic energy, as detailed in the Supporting Information.

For EMBs, we generate spherical meshes using icosahedral subdivision, resulting in a surface composed of 2562 vertices. For GVs, the structure is constructed by stacking concentric circles of particles in a staggered configuration, which are then smoothly tapered to form the conical end-caps, resulting in a mesh with 1404 vertices. This coarse-grained representation captures both the global geometry and local elastic properties of the membranes while remaining computationally efficient at the mesoscale.

2.3. Fundamental Scales. The solvent and encapsulated gas phases are modeled using DPD, which allows capturing relevant rheological properties, such as viscosity, on large spatiotemporal scales.[84] To parametrize the interactions between the various DPD beads, we first select the appropriate coarse-graining level, or equivalently, the length scale r_c. Due to the disparate sizes of EMBs, which can be as large as several micrometers, and GVs, where the diameter is at most several hundred nanometers, we use two different sets of fundamental scales (length, energy, and mass), specified in Table S1 of Supporting Information.

We choose the length scale r_c so that the radius of the particular object in the smallest dimension is at least 2 r_c. This is to ensure a large enough resolution of the immersed objects compared to the cutoff 1 r_c of the DPD interaction between the beads, eqs S79 and S80 of Supporting Information. The mass scale m is chosen to reproduce the density of the water/gas/shell and is calibrated, so that the mass of the water bead is equal to 1 m: $m = \rho_w^{exp} r_c^3/\rho_w$, where ρ_w is the number density of water beads and $\rho_w^{exp} = 997$ kg/m^3 is the physical density of water. For the energy scale ε, we take the thermal energy at room temperature $T_0 = 300$ K, $\varepsilon = k_BT_0$. The time scale τ follows from the other three fundamental scales

$$\tau = \sqrt{\frac{mr_c^2}{\varepsilon}} \tag{6}$$

We use the DPD parameters specified in Table 1. To keep the DPD system fluid-like and avoid the freezing artifacts appearing at $a_{\alpha\beta} \gtrsim 250\ k_BT_0/r_c$,[85−87] we use $a_{\alpha\beta} = 100\ k_BT_0/r_c$. For high coarse-graining levels, as is the case here, such a value of $a_{\alpha\beta}$ leads to a highly compressible liquid or equivalently a low value of the speed of sound c_0. Since we are interested in phenomena characterized by a low Mach number Ma = $u/c_0 \ll 1$, with u the typical particle velocity, this does not have a great impact on dynamics in this work.

We set the DPD interaction coefficients a_{wg}, a_{oo} and a_{og} in line with existing red blood cell models. We should note that setting a_{wg} and a_{og} to zero results in zero surface tension between the corresponding phases. The surface tension of the interfaces can be tuned by introducing an exponential conservative interaction between the beads of different phases,[88,89] however this is beyond the scope of the current paper. Additionally a_{gg} was set to zero to model the ideal gas with a linear pressure density relation, which we discuss in detail below in subsection "Inducing compression and buckling".

We have also ensured that the water/gas viscosity ratio is high by varying γ_{gg} and the kernel power k_{gg} in eq S80 of Supporting Information. Our choice of DPD parameters yields realistic viscosity ratios $\eta_w/\eta_{N2} \approx 63$ for water/nitrogen and $\eta_w/\eta_{air} \approx 48$ for water/air, which are close to the experimental values of $\eta_w/\eta_{N_2} \approx 51$ and $\eta_w/\eta_{air} \approx 48$.

2.4. Down-Scaling of Elastic Forces. At typical length scales r_c of the objects, the dimensionless values of the 2D Young's moduli are large, as they scale as $\sim r_c^2/\varepsilon$, i.e., physically, elastic energy is much larger than k_BT_0. To ensure computational feasibility, we scale down all elastic moduli in our simulations by a factor $f_{scale} \ll 1$. This preserves the so-called Föppl-von-Karman number FvK, which determines the shape of the objects in equilibrium[90,91]

$$\mathrm{FvK} = \frac{ER_0^2}{\kappa} \tag{7}$$

where E is the 2D Young's modulus, $\kappa \propto E$ is the bending constant, and R_0 is the typical radius of the object. Consequently, computed quantities such as critical stretching forces and buckling pressures must be divided by f_{scale}.

The behavior of elastic objects under shear flow is governed by the dimensionless capillary number[91,92]

$$\mathrm{Ca} = \frac{\eta\dot{\gamma}R_{eff}}{\mu} \tag{8}$$

To preserve it, the viscosity of water must also be scaled accordingly, $\tilde{\eta}_w = f_{scale}\eta_w$, where η_w is the physical viscosity of water.

We choose two different f_{scale} values corresponding to each unit set (Table S1), ensuring that $\kappa/(k_BT_0) > 10$ to prevent significant perturbation of the object by thermal fluctuations, which primarily originate from the solvent beads. For each unit set, the target viscosity $\tilde{\eta}$ is achieved by adjusting the values of γ_{ww} and k_{ww} (Table 1).

2.5. Fluid−Structure Interactions. The boundary conditions at the fluid-immersed structure interface have a large effect on the behavior of UCAs under nonequilibrium conditions, such as shear or

https://doi.org/10.1021/acsanm.5c02783
ACS Appl. Nano Mater. 2025, 8, 16053−16070

plug flow.[93] First, to prevent leakage of the solvent inside the gas vesicles or microbubble, we impose the no-through boundary condition by using the bounce-back mechanism, where the particles are introduced back based on the Maxwell distribution of velocities at temperature T_0.[94]

To control the velocity boundary conditions at the UCA−water or UCA−gas interface, one typically tunes the dissipative parameter γ_{ow} (γ_{og}) between the water (gas) and the UCA beads. A specific value of the dissipative parameter ensures the no-slip boundary condition[48]

$$\gamma_{o\{w,g\}} = \frac{2\tilde{\eta}_{\{w,g\}}(2k_{fsi}+1)(2k_{fsi}+2)(2k_{fsi}+3)(2k_{fsi}+4)}{3\pi r_c^4 \rho_{\{w,g\}}\rho_m} \tag{9}$$

where ρ_m is the area number density of the vertices of the immersed membrane, $\rho_{\{w,g\}}$ is the number density of the fluid (water or gas), $\tilde{\eta}_{\{w,g\}}$ is the corresponding scaled-down viscosity, and k_{fsi} is the kernel power of the dissipative weight function set to 0.5 for both unit sets. The complete DPD parameter sets used for UCA−water and UCA−gas interfaces are given in Table 1.

2.6. Inducing Compression and Buckling. According to the semiempirical equation of state eq 5, the fluid pressure is linearly proportional to a_{ww}, which is confirmed numerically (see Figure S9 in Supporting Information). Thus, water pressure is controlled by varying the interaction parameter a_{ww} between water beads linearly in time until it reaches a desired final value, where it remains for the second half of the simulation to allow the structure to relax into its final shape.

Unlike that of water, the compressibility of the gas phase plays an important role, significantly affecting the shell's collapse pressure. At the buckling transition, the dominant deformation mode is determined by the bending constant (which is small for thin shells) and is thus sensitive to the compressibility of the interior gas. At realistic pressure, the compressibility of DPD gas, as follows from the DPD equation of state eq 5, is anomalously low. To remedy this, we model the gas phase as ideal by setting the interactions between gas beads to 0, which also aligns with the ideal gas behavior in the relevant temperature and pressure range. Consequently, the resulting DPD gas pressure is extremely low. To ensure mechanical stability, it is compensated by applying an outward force to each triangular face of the shell, evenly distributed among its three vertices to ensure zero torque on the triangle: $\mathbf{f}_p = -pA\mathbf{n}/3$, where A and $\mathbf{n}$ are the area and inward-pointing normal of the triangle (see Supporting Information S2), and p is the desired pressure compensation.

2.7. Open-Boundary Molecular Dynamics. To perform nonequilibrium simulations we use open-boundary molecular dynamics (OBMD),[95−97] which allows imposing momentum and/or heat fluxes at the system's boundaries. A typical OBMD setup consists of three fundamental parts: a central domain—the region of interest (ROI), and two buffer regions in which particle deletion or insertion is performed. The particle number in the buffer regions is controlled by a feedback algorithm

$$\Delta N = -\frac{\Delta t}{\tau_B}(N - \alpha_B N_0) \tag{10}$$

where ΔN is the number of particles to be deleted ($\Delta N < 0$) or inserted ($\Delta N > 0$), Δt and τ_B are the time step and relaxation time of the buffers, N and N_0 the current and equilibrium particle numbers in either buffer, and α_B an empirical customized parameter. Particle insertion is facilitated by the USHER algorithm,[98] which employs an iterative steepest descent scheme on the potential energy surface.

OBMD imposes boundary conditions by adding external forces $\mathbf{f}_i$ to all buffer particles i, determined from the momentum balance

$$\mathbf{J}A\cdot\mathbf{n} = \sum_i \mathbf{f}_i + \sum_{i'} \frac{\Delta(m_{i'}\mathbf{v}_{i'})}{\Delta t} \tag{11}$$

where $\mathbf{J}$ is the momentum current density tensor, A the surface area of the interface between the buffer and the ROI, and $\mathbf{n}$ the normal to this interface pointing toward the center of the ROI. The second sum in eq 11 stands for the momentum gain or loss upon insertion or deletion of particles i' in the current time step. The momentum flux across the buffer−ROI interface is dictated by the desired boundary condition for the stresses, e.g. on boundaries with normals $\mathbf{n} = \pm\hat{\mathbf{e}}_x$

$$\mathbf{J}\cdot\mathbf{n} = P_{xx}\mathbf{n} + P_{yx}\hat{\mathbf{e}}_y + P_{zx}\hat{\mathbf{e}}_z \tag{12}$$

where P_{xx} is the equilibrium pressure, and P_{yx}, P_{zx} the shear stress components.

2.8. Quasiharmonic Analysis. In the analysis of molecular dynamics simulations of biomolecules, extracting eigenmodes and their frequencies is essential. The well-established method for this is quasiharmonic analysis,[99−101] also sometimes referred to as principal component analysis (PCA).[102] This approach is not limited to molecules but can also be applied to coarse-grained models of elastic objects, such as carbon nanotubes,[103,104] and in our case to UCAs.

The thermalized equilibrium configurational probability distribution of membrane vertices is given by

$$P(\mathbf{x}) = \frac{e^{-\beta E(\mathbf{x})}}{\int e^{-\beta E(\mathbf{x})}\,\mathrm{d}\mathbf{x}} \tag{13}$$

where $E(\mathbf{x})$ is the potential energy of the configuration expressed by a supervector $\mathbf{x}$ of particle coordinates, and $\beta = 1/(k_B T_0)$. In the quasiharmonic approximation, the potential energy surface is assumed to be a quadratic function $E(\mathbf{x}) \approx E(\langle\mathbf{x}\rangle) + \frac{1}{2}(\mathbf{x}-\langle\mathbf{x}\rangle)^T\mathbf{V}(\mathbf{x}-\langle\mathbf{x}\rangle)$, where $V_{ij} = \frac{\partial^2 E}{\partial x_i \partial x_j}$ is the Hessian, and $\langle . \rangle$ denotes thermal average, which is in our case calculated as a time-average of the vertex positions. Within this approximation, the configurational probability function takes the form of a multivariate Gaussian distribution and therefore the Hessian can be extracted from the trajectory through the covariance matrix $\Sigma_{ij} = \langle(x_i - \langle x_i\rangle)(x_j - \langle x_j\rangle)\rangle$ of particle coordinates

$$\mathbf{V} = k_B T_0 \boldsymbol{\Sigma}^{-1} \tag{14}$$

In determining Σ, we subtract the motion of the center of mass of the object and remove rotational motion using a trajectory alignment algorithm from the MDAnalysis Python package.[105,106] This algorithm finds the optimal rotation matrix between the current and reference configurations by minimizing the root-mean-square deviation between the configurations.[107,108]

Ignoring the damping coming from the solvent and the gas, the equation of motion reads

$$\mathbf{M}\ddot{\mathbf{x}} + \mathbf{V}\mathbf{x} = 0 \tag{15}$$

where $\mathbf{M}$ is the diagonal mass matrix, $\mathbf{M} = m\mathbf{I}$ in our case. Using the ansatz $\mathbf{x} = \mathbf{x}_0 e^{i\omega t}$, one obtains the generalized eigenvalue problem

$$\left(\boldsymbol{\Sigma} - \frac{k_B T_0}{\omega^2}\mathbf{M}^{-1}\right)\mathbf{x}_0 = 0 \tag{16}$$

which can be recast into a standard eigenvalue problem by defining $\mathbf{q}_0 = \sqrt{\mathbf{M}}\mathbf{x}_0$ and $\boldsymbol{\Sigma}' = \sqrt{\mathbf{M}}\boldsymbol{\Sigma}\sqrt{\mathbf{M}}$

$$(\boldsymbol{\Sigma}' - \lambda'\mathbf{I})\mathbf{q}_0 = 0 \tag{17}$$

where the eigenfrequencies of the structural vibrations

$$\omega = \sqrt{\frac{k_B T_0}{\lambda'}} \tag{18}$$

are obtained from the eigenvalues λ'.

3. RESULTS AND DISCUSSION

3.1. General Particle-Based Elasticity Framework for Simulating Membrane-Encapsulated Soft- and Biomaterials. The role of membranes in soft- and biomaterials is multifaceted. For biological cells, the membrane separates the interior from external disturbances and can also provide means for the exchange of ions, solvents, gas molecules, and other

https://doi.org/10.1021/acsanm.5c02783
ACS Appl. Nano Mater. 2025, 8, 16053−16070

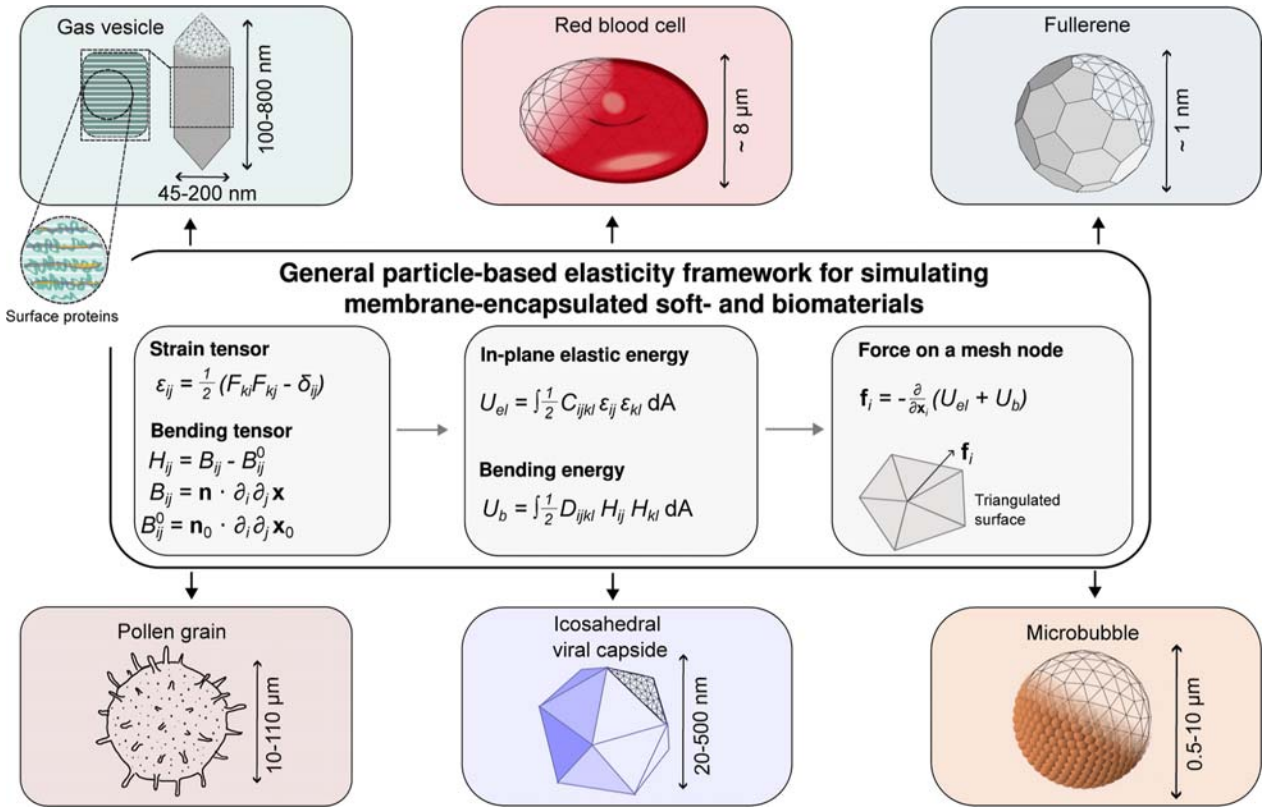

Figure 1. Overview of particle-based elastic modeling of thin shells used in this work. An object is described by its subunits and a triangulated network. Elastic energy is split into two parts: in-plane elastic energy, characterized by the material elastic tensor C_{ijkl} and the strain tensor ε_{ij} measuring the deformations; and bending energy, characterized by the flexural rigidity tensor D_{ijkl} and the bending tensor H_{ij}. The corresponding vertex forces are calculated by taking derivatives of the total elastic energy with respect to vertex positions. The modeling framework is applicable to biomaterials of different shapes and general local anisotropy.

substances.[109] Biological membranes typically consist of lipid, polymer, or protein units. The type of these units, their interaction with each other and the environment, as well as their bonding topology dictate the elastic behavior of membranes.

This extreme diversity of membranes with different elastic properties requires a general methodology that is capable of incorporating various possible symmetries, for example, the isotropic elasticity of EMBs on one hand, and orthotropic elasticity of GVs on the other. There are different approaches to modeling elastic properties of thin shells. A popular one is connecting the various subunits with harmonic bonds or potential wells, aided by a harmonic angular potential.[110] It is well-known that a straightforward application of such an approach—using harmonic bonds with equal spring constants—does not lead to general elastic behavior.[111] An alternative approach, which we follow here, is to discretize the continuum elastic surface energy on a triangulated surface spanned by the various subunits (see Figure 1).[112] This energy expression is then used in the subsequent per-vertex force calculations.

We quantify the deformation using the deformation gradient $F_{ij} = \frac{\partial x_i}{\partial x_{0j}}$, which relates the difference in positions of two infinitesimally close material points in the deformed configuration $\mathbf{x}$ to their difference in the reference configuration $\mathbf{x}_0$.[113] To exclude local rotation, deformation is typically described using the Green-Lagrange deformation tensor (strain tensor) $\boldsymbol{\varepsilon} = \frac{1}{2}(\mathbf{F}^T\mathbf{F} - \mathbf{I})$, which measures the deformation relative to the reference configuration. Moreover, we incorporate anisotropic elasticity to model the diverse and generally complex elastic properties of biological membranes. Anisotropic objects are characterized by their reduced symmetry group or equivalently by a set of structural tensors $\mathbf{M}$, which reflect the distinguished directions, lines, or planes of an object. See Supporting Information for a detailed overview of the effects of material symmetry and the principle of isotropy of space on the form of the elastic energy.

In linear elastic theory of thin shells, in-plane and bending deformations are decoupled, and the total elastic energy is $U = U_{el} + U_b$, where U_{el} and U_b are the in-plane elastic and bending energies, respectively.

The general in-plane elastic energy is formulated using the two-dimensional (2D) in-plane strain tensor $\boldsymbol{\varepsilon}$

$$U_{el} = \int \frac{1}{2} C_{ijkl} \varepsilon_{ij} \varepsilon_{kl} dA \tag{19}$$

where dA is the surface element of the shell, and $C_{ijkl} = hC^{3D}_{ijkl}$ is its in-plane elastic tensor, derived from the three-dimensional (3D) material elastic tensor C^{3D}_{ijkl} and the shell thickness h, eq S6 in Supporting Information. The in-plane stress tensor $\sigma_{ij} = C_{ijkl}\varepsilon_{kl}$ has units of force per unit length. The tensor C_{ijkl} satisfies $C_{ijkl} = C_{jikl} = C_{ijlk}$, which reflects the symmetries of the strain and stress tensors. Under the assumption of hyperelasticity, where stress is derived from an elastic potential, it also satisfies $C_{ijkl} = C_{klij}$. These symmetries reduce the

https://doi.org/10.1021/acsanm.5c02783
ACS Appl. Nano Mater. 2025, 8, 16053−16070

maximum possible number of elastic parameters from 81 to 21 in 3D and from 16 to 6 in 2D. The in-plane elastic tensor C_{ijkl} is expressed as a combination of Kronecker delta δ_{ij} and in-plane structural tensor(s) M_{ij}, as derived in Supporting Information in the context of orthotropic elasticity of GVs.

A general form of the bending energy is

$$U_b = \int \frac{1}{2} D_{ijkl} H_{ij} H_{kl} \mathrm{d}A \tag{20}$$

where $H_{ij} = B_{ij} - B^0_{ij}$ is the bending tensor,[114] which measures the deviation of the curvature tensor $B_{ij} = \mathbf{n} \cdot \partial_i \partial_j \mathbf{x}$ in the deformed state from the spontaneous curvature tensor $B^0_{ij} = \mathbf{n}_0 \cdot \partial_i \partial_j \mathbf{x}_0$. Here, $\mathbf{n}$ and $\mathbf{n}_0$ denote the normals to the deformed ($\mathbf{x}$) and undeformed ($\mathbf{x}_0$) configuration surfaces, respectively. The principal directions of the curvature tensor align with extremal curvatures, represented by its eigenvalues $1/R_1$ and $1/R_2$, where R_1 and R_2 are the principal radii of curvature. In linear thin shell elasticity, the material flexural rigidity tensor D_{ijkl} is fully specified by the material elastic tensor through the relation $D_{ijkl} = \frac{h^3}{12} C^{3D}_{ijkl} = \frac{h^2}{12} C_{ijkl}$, eq S7 in Supporting Information.

In the constant strain triangle approximation (CST),[115] where the strain field ε is assumed to be constant within each triangle, the surface integrals eqs 19 and 20 can be replaced by summation over the triangles of the triangulated surface, as given in eqs S8 and S33 of Supporting Information.

3.2. Models of Ultrasound Contrast Agents. Within the introduced general elastic particle-based computational framework, we focus on modeling the behavior of two encapsulated agents: EMBs and GVs. The specific models we employ are inspired by RBC membrane models.[40,41,43,44,47,49−51,54,55,91,116−118] The RBC membrane consists of two main components: a pseudohexagonal elastic spectrin network,[119] and a fluid-like lipid bilayer. In contrast, polymer- or protein-based EMBs and GVs comprise only an elastic network,[29] while lipid-based microbubbles are encapsulated by a lipid monolayer membrane.[72] The primary differences in modeling EMBs and GVs compared to RBCs lie in the different topology of the triangulated surfaces and, in the case of GVs, the inclusion of anisotropic elastic terms.

3.3. Microbubbles. EMB shells are made of proteins, polymers, or lipids. Most EMBs appear to be well described by an isotropic elastic model,[120] although there are continuum models that assume transversely isotropic elastic shells where the anisotropy axis is along the radial direction.[121]

The elastic tensor C_{ijkl} of isotropic materials is exclusively expressed through the isotropic tensor—the Kronecker delta δ_{ij}. It has two independent terms

$$C_{ijkl} = K_a \delta_{ij} \delta_{kl} + \mu(\delta_{ik}\delta_{jl} + \delta_{il}\delta_{jk} - \delta_{ij}\delta_{kl}) \tag{21}$$

where K_a and μ are the bulk and the shear moduli, respectively. There is a more detailed description of the elastic moduli and the expression for elastic energy in Supporting Information.

The bending energy follows from eq 20 and, for isotropic shells, consists of two independent terms

$$U_b = \int \left[\frac{1}{2} \kappa J_1^2 - \kappa(1-\nu) J_2 \right] \mathrm{d}A \tag{22}$$

where $\kappa = \frac{Eh^2}{12(1-\nu^2)}$ is the bending constant, E, ν are the 2D Young's modulus and Poisson's ratio (eqs S20 and S21 in Supporting Information), and the scalar differential curvature invariants are defined as $J_1 = \mathrm{tr}(\mathbf{H})$ and $J_2 = \frac{1}{2}[\mathrm{tr}(\mathbf{H})^2 - \mathrm{tr}(\mathbf{H}^2)] = \det(\mathbf{H})$. The bending energy eq 22 is discretized using the Kantor-Nelson approach, see Supporting Information.

3.4. Gas Vesicles. The GV membrane consists of GvpA protein ribs arranged helically around the GV axis,[34,36] see Figure 1. Its elastic properties differ along the ribs and perpendicular to them.[34,65] The local material symmetry group $\mathcal{G}$ is therefore orthotropic, spanned by four elements: identity, inversion and a pair of reflections across the rib direction and perpendicular to it. The 2D elastic tensor can therefore be constructed using Kronecker delta δ_{ij} and one structural tensor, which is invariant to all group elements in $\mathcal{G}$: $\mathbf{M} = \mathbf{m} \otimes \mathbf{m}$, where $\mathbf{m}$ is chosen to point perpendicular to the rib. Since the ribs run nearly perpendicular to the GV axis, $\mathbf{m}$ is well approximated by a projection (see Supporting Information).

Taking into account this symmetry, the most general form of the elastic tensor is

$$\begin{aligned} C_{ijkl} &= K_a \delta_{ij}\delta_{kl} + \mu(\delta_{ik}\delta_{jl} + \delta_{il}\delta_{jk} - \delta_{ij}\delta_{kl}) \\ &\quad + (\mu_L - \mu)(m_i m_l \delta_{jk} + m_j m_l \delta_{ik} + m_i m_k \delta_{jl} + m_j m_k \delta_{il}) \\ &\quad + c m_i m_j m_k m_l, \end{aligned} \tag{23}$$

with $\mu_L > 0$, $c > 0$[122,123] the anisotropic elastic coefficients, which are positive for stability reasons. The coefficient μ_L is the membrane's (in-plane) shear elastic constant, while c contributes to the stiffness along the anisotropy axis $\mathbf{m}$.[124] A more in-depth explanation regarding the in-plane elastic energy is provided in Supporting Information. Our construction of the elastic tensor assumes isolated, fully formed shells with a fixed equilibrium helical arrangement of GvpA proteins. Modeling of the elastic properties of GVs during the biogenesis or under variable temperature conditions, where the shell is forming through dynamic self-assembly of GvpA proteins, is beyond the scope of this paper.

In the linear regime, the coefficients K_a, μ, μ_L, and c in eq 23 can be related to the engineering constants: Young's modulus along the GV axis, E_l, and perpendicular to it (along the ribs), E_t, Poisson's ratio ν_{lt} for stretching along the ribs, and shear modulus $G(=\mu_L)$. The other Poisson's ratio ν_{tl} is already fixed with these choices. These relations are given in eqs S24−S31 of S1.

Following eq 20, the bending energy of a thin orthotropic shell can be expressed as a sum of four independent terms

$$U_b = \int \left(\frac{1}{2}\kappa_t J_1^2 - \kappa_t(1-\nu_{lt}) J_2 + \kappa_\mu J_3 + \frac{1}{2}\kappa_c J_4^2 \right) \mathrm{d}A \tag{24}$$

where new scalar differential curvature invariants are defined as $J_3 = \mathbf{m}^T \mathbf{H}^T \mathbf{H} \mathbf{m}$, $J_4 = \mathbf{m}^T \mathbf{H} \mathbf{m}$, and $\kappa_t = \frac{E_t h^2}{12(1-\nu_{lt}\nu_{tl})}$, $\kappa_\mu = \frac{(\mu - \mu_L)h^2}{6}$, $\kappa_c = \frac{ch^2}{12}$ are the bending constants in the thin shell regime.[125]

For simplicity, we keep the bending energy of the GV membrane isotropic in this work and set the bending constant to $\kappa = \frac{E_t h^2}{12(1-\nu_{lt}^2)}$, where we have used the smaller Young's modulus E_t. This is to ensure that the circumferential instability, which in buckling experiments occurs at lower pressure amplitudes than other more complicated instabilities, has the correct energy cost.

https://doi.org/10.1021/acsanm.5c02783
ACS Appl. Nano Mater. 2025, 8, 16053−16070

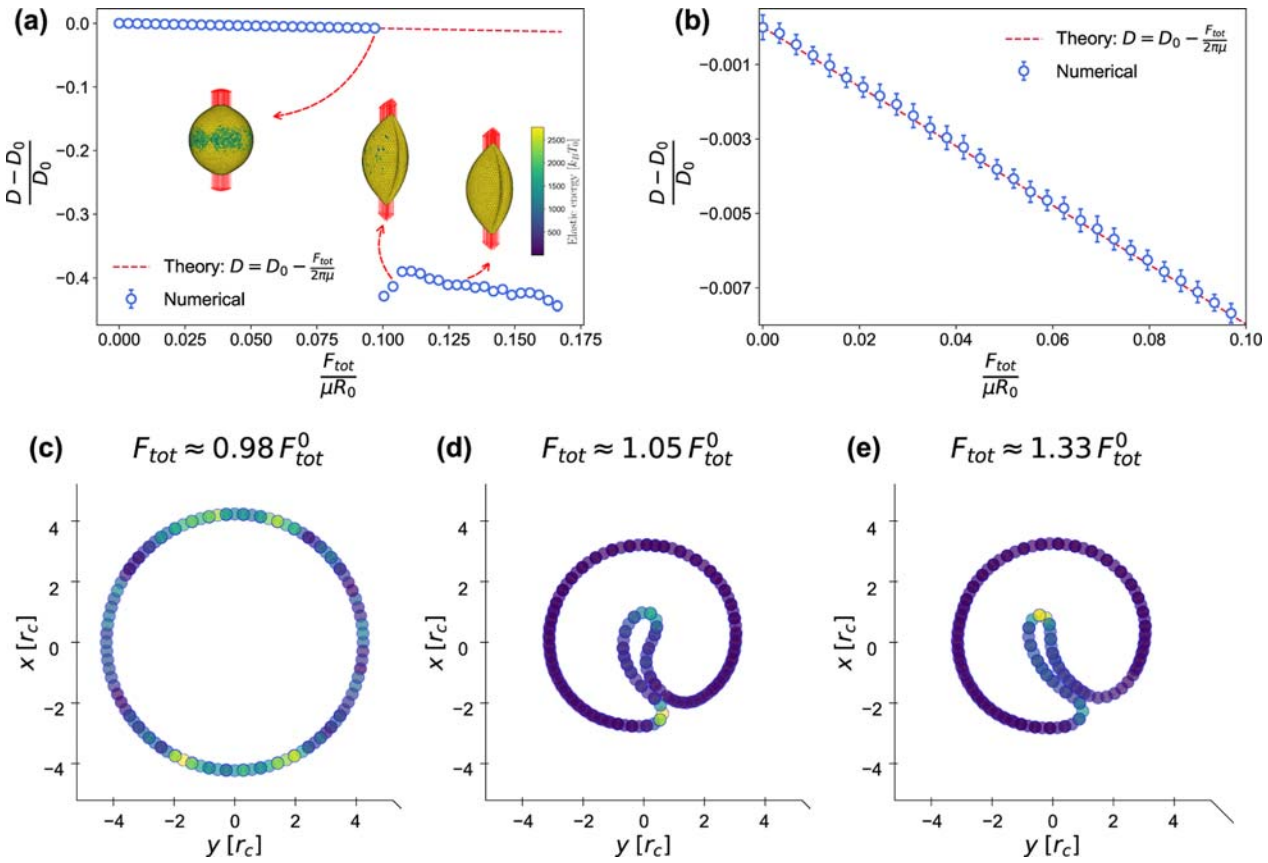

Figure 2. EMB stretching. (a) Relative EMB diameter change as a function of applied force F_{tot} in units of μR_0. (b) Small-strain part of the dependence in (a), compared to eq 25. (c−e) Equatorial slices of EMBs perpendicular to the stretching direction at values of F_{tot}, corresponding to the three regimes in (a); $F^0_{tot} = 0.099\ \mu R_0$. The coloring in the side views (a) the top views (c−e) represents local elastic energy. Equatorial slices (c−e) are single-particle thick.

3.5. Mechanical Properties. Mechanical properties of biomaterials can be determined by performing elementary mechanical experiments, such as stretching,[126] torsion,[127] and compression.[128] Stretching experiments are typically done using optical tweezers, where two micrometer-sized spherical silica beads are attached to the ends of a particle and then moved in opposite directions. The experimental data consist of force−displacement curves, which can be translated to stress−strain curves under certain assumptions.

We conducted stretching, compression/buckling, and torsion simulations of EMBs and GVs. The stretching force−displacement curves of our model EMBs and GVs were determined by adding oppositely equal forces to a small set of diametrically opposite vertices of their membrane. The GV torsion simulations were performed by rotating the GV cylinder ends in opposite directions, Figure S7. In principle, this could be achieved experimentally with an angular optical tweezer device, which is a relatively new methodology.[129,130]

We also derive analytical results for the stretching, torsion, and compression in the small deformation limit and verify their validity by simulations.

3.6. Microbubble Stretching. We model the stretching experiment by uniformly distributing the stretching forces over 64 vertices at each pole of an EMB (approximately 2.5% of all the vertices). This is equivalent to a contact diameter of approximately 0.65 μm, which falls within a range of typical silica bead sizes used in optical tweezer experiments. As shown in Figure 2a, the stretching of an EMB results in a decrease in diameter D perpendicular to the stretching direction. For small strains, one finds (eq S65 of Supporting Information)

$$D = D_0 - \frac{F_{tot}}{2\pi\mu} \tag{25}$$

where F_{tot} is the total force applied to the ends of the EMB, and $D_0 = 2R_0$ is its equilibrium diameter. As seen in Figure 2a,b, the measured diameter perpendicular to the stretching direction matches excellently with eq 25 in the regime of small strains. The expression eq 25 differs from the result for an elastic disc, which is often used to model red blood cell stretching in the linear regime:[131] $D = D_0 - \frac{F_{tot}}{2\pi\mu}\left[1 - \left(1 - \frac{\pi}{2}\right)\frac{\mu}{K_a}\right]$.

Above $F_{tot} \approx 0.099\ \mu R_0$, the EMB undergoes a transition into a circumferentially wrinkled shape and the diameter, calculated as twice the average distance of equatorial particles from their center of mass, drops significantly.

The onset of this wrinkling transition can be understood as a trade-off between compression in the circumferential direction and out-of-plane bending deformation. When stretching is applied, the shell initially accommodates the deformation through in-plane stretching and accompanying in-plane compression in the equatorial direction. Eventually, this compression becomes too costly and destabilizes. At this point the shell reduces the compression energy by buckling.

One can also notice an azimuthally nonuniform distribution of energy of the equatorial slice in Figure 2c. These variations

https://doi.org/10.1021/acsanm.5c02783
ACS Appl. Nano Mater. 2025, 8, 16053−16070

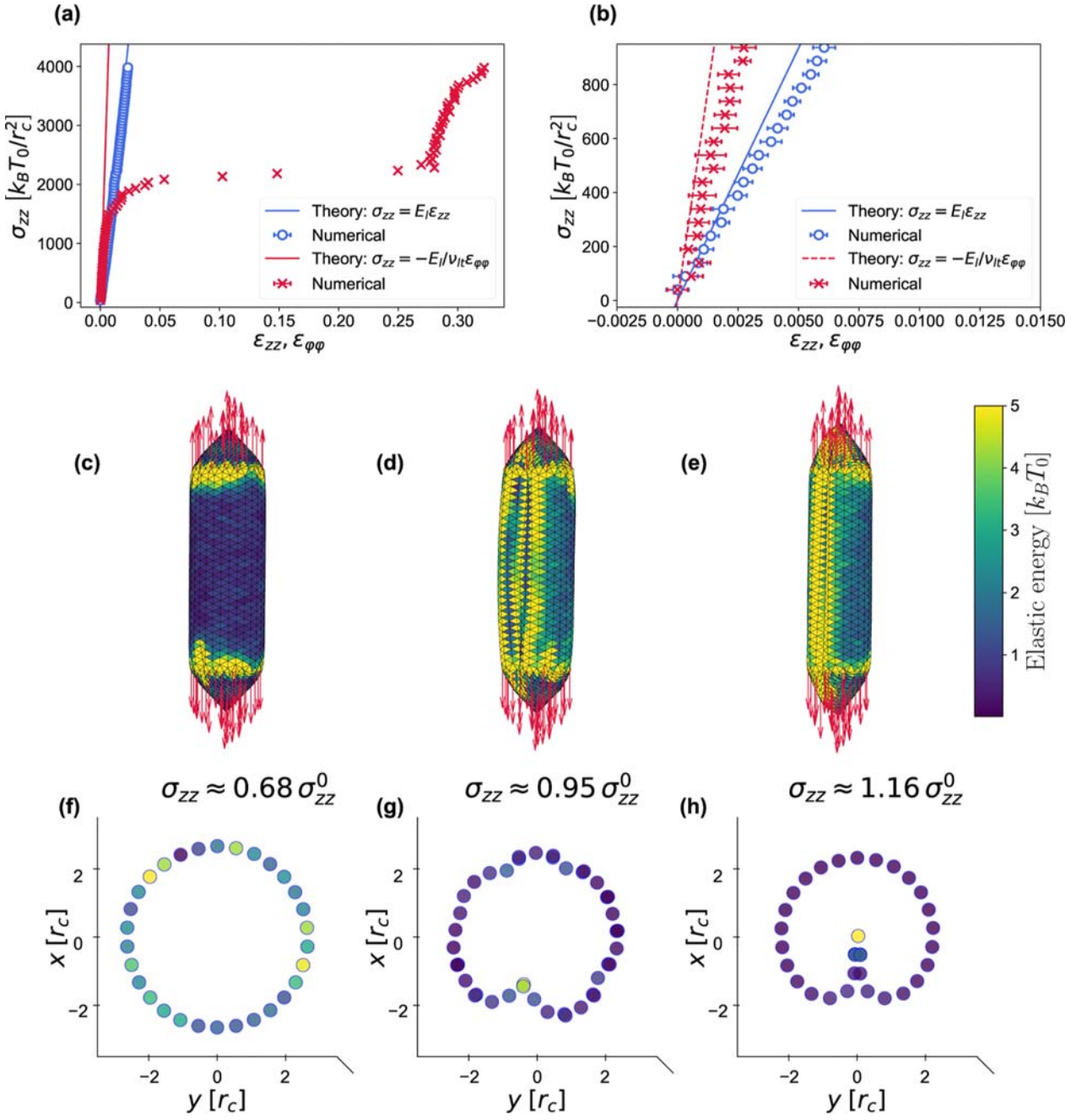

Figure 3. GV stretching. (a) Stress σ_{zz} as a function of longitudinal strain ε_{zz} and circumferential strain $\varepsilon_{\varphi\varphi}$ for a GV stretched along its axis. (b) Comparison with eqs S74 and S75 of Supporting Information in the limit of low strain. (c–e) Side views and (f–h) central xy slices of the GV at different values of σ_{zz}, with $\sigma_{zz}^0 = 2184\ k_BT_0/r_c^2$. The coloring represent local elastic energy. To better depict the first buckling transition, slice (g) is taken at a height of 4 r_c from the GV center. Central slices (f–h) are single-particle thick.

appear random and reflect the fluctuations in the membrane as it approaches the wrinkling transition.

3.7. Gas Vesicle Stretching. We examine the response of a GV to stretching along its axis (z axis), Figure 3, which should be the most feasible experimentally. In these simulations we distribute the stretching forces uniformly over all vertices of the conical parts. For small stretching forces, the length of the GV increases linearly, while its diameter in the xy plane decreases, in line with simple linear elastic response. The stress–strain response of a GV can be estimated by considering the uniaxial stress in its cylindrical part, $\sigma_{zz} = \frac{F_{tot}}{2\pi R}$, and the corresponding strain along z, $\varepsilon_{zz}=(H_{cyl} - H_{cyl}^0)/H_{cyl}^0$, where H_{cyl} and H_{cyl}^0 are the heights of the GV cylinder in the deformed and reference configurations, respectively. The circumferential strain, on the other hand, is deduced from the relative radius change, $\varepsilon_{\varphi\varphi} = (R - R_0)/R_0$, where R and R_0 are the radii in the deformed and reference configurations, respectively. It is important to emphasize that H_{cyl} is measured between the ends of the cylindrical section, excluding the conical parts, where the stress depends on z as the radius tapers from R to 0. Figure 3a,b shows that the linear response matches excellently with the constitutive equations eqs S74 and S75 of Supporting Information. Measurement of this small-strain response could

https://doi.org/10.1021/acsanm.5c02783
ACS Appl. Nano Mater. 2025, 8, 16053–16070

therefore be used to estimate both the longitudinal Young's modulus E_l and the Poisson's ratio ν_{lt}.

At a certain point, the GV buckles, forming a dimple, localized to each end of the cylindrical part, see Figure 3d,g. The onset of these dimples is already seen in Figure 3c which shows an azimuthally nonuniform distribution of energy at the ends of the cylindrical parts. At a larger longitudinal stress $\sigma_{zz}^0 \approx 2184 k_B T_0 / r_c^2$, the GV buckles into a shape with a single dimple along the entire length, Figure 3e,h. The onset of this instability is analogous to that in the stretching of EMBs—the circumferential compression of the GV reaches a point, where out-of-plane bending is energetically favorable. This transition is also accompanied by a large jump in the circumferential strain $\varepsilon_{\varphi\varphi}$. Interestingly, the longitudinal strain ε_{zz} keeps increasing linearly with σ_{zz} without a large discontinuity.

3.8. Compression. In compression experiments, the external fluid pressure is increased and the corresponding volume change of the body is measured. In simulations, the pressure increase Δp is controlled by varying the interaction parameter a_{ww} (eq 1) between the water beads.

For low Δp, the volume change can be obtained analytically for both EMBs and GVs by calculating the stresses $\sigma_{\theta\theta}$ and $\sigma_{\varphi\varphi}$, depicted in Figures 4 and 5. Neglecting the compressibility

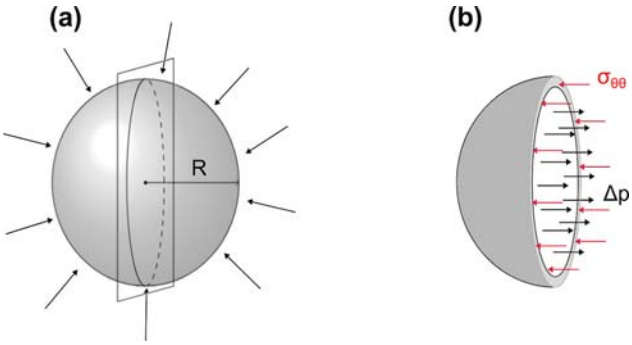

Figure 4. Pressure-induced stress in the EMB membrane. (a) EMB in a pressurized environment, exerting uniform compression forces. (b) Differential pressure force on the hemisphere (black arrows) in equilibrium with elastic force of the shell (red arrows).

modulus of the trapped gas and the membrane bending contributions, which are negligible in the regime of low deformation, the volume strain of an EMB is (eqs S66–S71 of Supporting Information)

$$\frac{\Delta V}{V_0} = -\frac{3(1-\nu)R_0}{2E}\Delta p = -\frac{3R_0}{4K_a}\Delta p \tag{26}$$

which is confirmed numerically in Figure 6a,b.

For a GV with orthotropic elasticity, the volume strain depends on both Young's moduli E_l and E_t, and the Poisson's ratio ν_{lt} (eqs S76–S78 of Supporting Information)

$$\frac{\Delta V}{V_0} = -\frac{R_0}{2E_l}\left(1 - 4\nu_{lt} + 4\frac{E_l}{E_t}\right)\Delta p \tag{27}$$

which is again confirmed numerically in Figure 7a,b. The linear weak-compression slope was also observed experimentally by Walsby[132] using a glass compression tube and was used to estimate the bulk modulus of GVs. In the isotropic case, where $E_l = E_t$, eq 27 agrees with the well-known result for isotropic

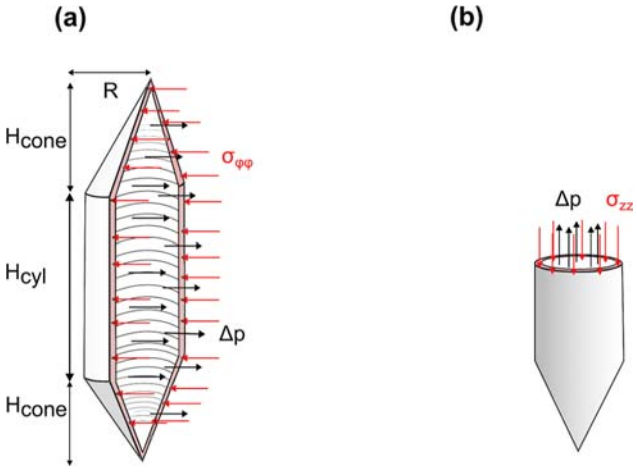

Figure 5. Pressure-induced stress in the GV membrane. GV in a pressurized environment: (a) meridional stress $\sigma_{\varphi\varphi}$ caused by differential pressure on the longitudinal cross-section, and (b) equatorial stress σ_{zz} caused by differential pressure on the transverse cross-section.

cylindrical shells,[133] which is often used to estimate the Young's modulus of GVs.[29,132]

In the small deformation regime governed by the membrane in-plane elasticity, as described by eqs 26 and 27, the effective compressibility of the shell increases linearly with its size R_0. The shape of the shell also plays an important role. There is a distinct difference between the compression of the spherical EMB and the cylindrical GV with the same radius. For the same shell material, i.e., $E_l = E_t = E$, $\nu_{lt} = \nu$, eq 27 gives $\frac{\Delta V}{V_0} = -\frac{(5-4\nu)R_0}{2E}\Delta p$, which should be compared with eq 26. Thus, for the same shell material and radius, the cylinder has almost twice the compressibility of the sphere.

3.9. Buckling. GVs are known to produce nonlinear acoustic signals when exposed to high-amplitude ultrasound pulses[20]—at such pressure amplitudes, they buckle reversibly. By measuring optical density as a function of pressure, the buckling pressures were experimentally determined for a wide range of GV sizes and diameters. We investigate buckling instabilities of EMBs and GVs by increasing the solvent pressure beyond the small strain limit.

Examples of EMB buckling are shown in Figure 6c–e. An analytical expression for the critical buckling pressure of spherical shells exists, eq S73 in Supporting Information, which is in an excellent agreement with our simulations, see Figure S6 in Supporting Information. It involves an empirical correction factor due to imperfections of the shell, which consistently takes on a well-defined value also for our model EMB. We also performed dynamic numerical buckling experiments at various pressure increase rates. While the buckling pressure remains nearly unchanged across different rates, the structure evolves through different intermediate shapes, from a single indentation for the slowest pressure increase to multiple lobes when the pressure increases more abruptly, which is in line with the numerical simulations of ref 134.

For GVs, we compare the predicted buckling pressure to the hydrostatic critical pressure in ref 66, which considers isolated *H. salinarum* GVs in a solution. At a pressure of about $\Delta p^0 \approx 31.0\ k_B T_0 / r_c^3$, our GV buckles into a shape with three lobes along the circumference, Figure 7d,g. Reverting to physical

https://doi.org/10.1021/acsanm.5c02783
ACS Appl. Nano Mater. 2025, 8, 16053–16070

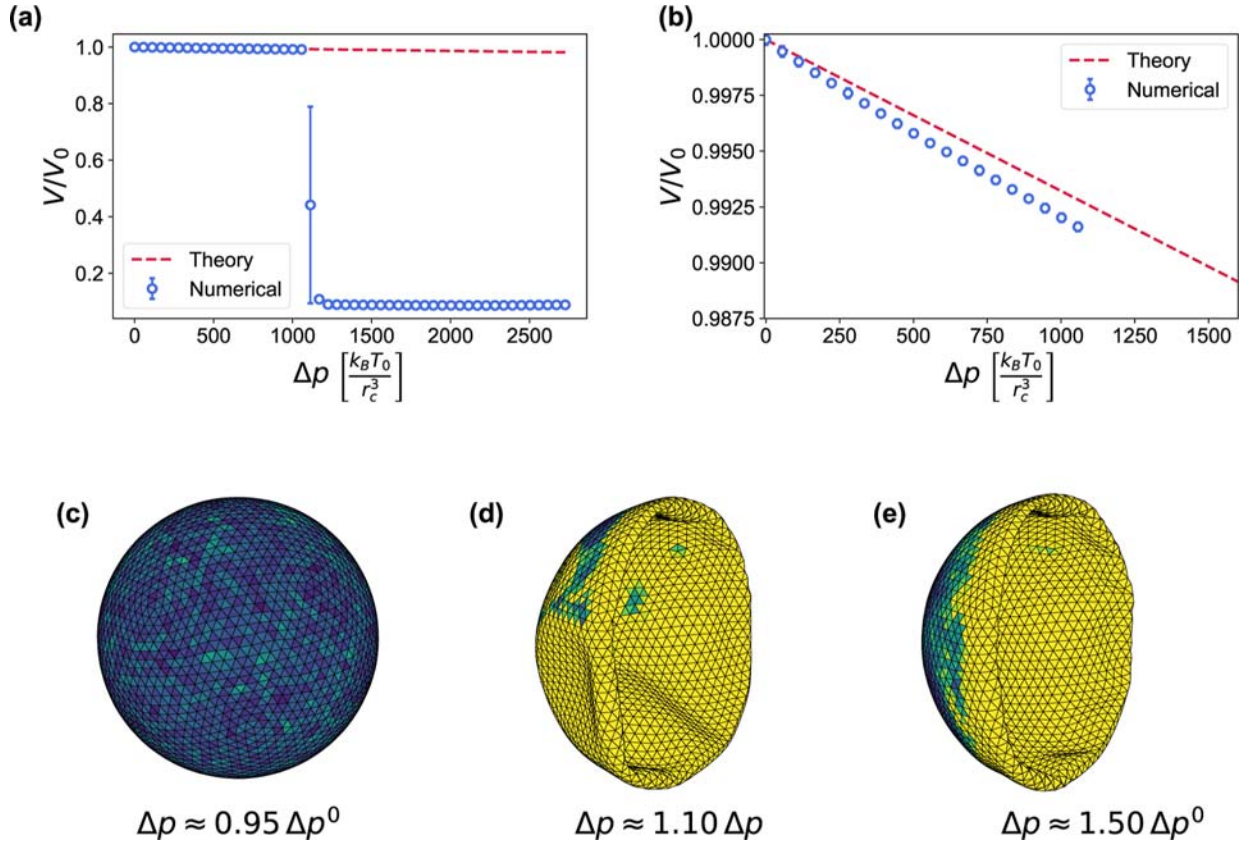

Figure 6. EMB compression and buckling. (a) Relative volume change of an EMB due to the external pressure increase Δp, compared to eq 26 (red dashed line). (b) Closeup of (a) in the small deformation regime. (c–e) Compressed EMB at different values of Δp, with $\Delta p^0 = 1113\ k_B T_0/r_c^3$ the buckling threshold pressure. Local buckling nucleations are noticeable in (c), while (d,e) show fully buckled states. The coloring represents local elastic energy.

units and up-scaling by f_{scale} (see Methods and Table S1), $\Delta p^0 \approx 37.9$ kPa. This is below the value of 64 kPa in ref 66. It is also significantly below experimental values of refs 19 and 64 of about $\Delta p^0 \approx 200$ kPa and $\Delta p^0 \approx 178$ kPa, respectively. One possible reason for the discrepancies with refs 19 and 64 is that these experiments used acoustic waves to induce the GV collapse, which is known to yield higher measured collapse pressures than hydrostatic techniques. A general reason is that the actual bending constant κ is an independent parameter, lower than predicted by thin-shell theory—a single molecular layer membrane can hardly be considered a continuum across its thickness. Another possible reason is that the nonlinear elastic coefficients a_3, a_4, b_1 and b_2 (see Supporting Information), which we neglected in this work, could play an important role in large deformations, such as buckling. Optimal values of these nonlinear elastic coefficients and their uncertainties could be estimated directly from experimental measurements using hierarchical Bayesian uncertainty quantification,[91] which will be addressed in our future work.

At an even higher pressure of $\Delta p \approx 58\ k_B T_0/r_c^3 \approx 71$ kPa, the GV undergoes a transition into a two-lobe shape, Figure 7e,h, which is actually closer to the collapse pressure in ref 66. This particular shape was also obtained via a linear buckling analysis by Salahshoor et al.[65] Both buckling shapes are corroborated by the existence of two low-frequency vibrational modes of similar shape, which are calculated in the next section.

Our buckling simulations were conducted under quasi-static conditions, where pressure was increased slowly to mimic low-frequency ultrasound or static compression experiments. While this approach provides valuable insight into mechanical thresholds, it does not capture the effects of rapid acoustic pressure fluctuations typical of therapeutic ultrasound. Extending the framework to incorporate dynamic loading and cavitation phenomena—potentially through reactive force fields—remains an important direction of our next steps.

3.10. Vibrational Modes. Finding the right ultrasound frequency is key for optimal tissue imaging,[135] as well as for inducing sonophoresis and affecting drug carrier behavior in terms of growth, oscillations, rupture, and drug release via cavitation.[136] Here, we study the low-frequency modes of GVs that could play a major role in ultrasound backscattering phenomena.

To extract the eigenmodes and their corresponding eigenfrequencies, we run a long simulation of 4000 τ (eq 6, Table S1) of a GV surrounded by DPD water and perform principal component analysis (PCA) on the trajectories of the GV vertex beads, see Methods. Some of the extracted low-frequency modes are shown in Figure 8a–f.

In the relevant regime, where the GV cylinder is longer than the end cones, the lowest-frequency modes are largely confined to the cylindrical region, as highlighted by Figure 8h. Consequently, the ends of the cylinder impose an effectively rigid boundary condition. In this regime, the modes can be classified not only according to their circumferential number n, but also their axial number m, on top of their polarization branch, Figure 8a–f. They follow considerably well the

https://doi.org/10.1021/acsanm.5c02783
ACS Appl. Nano Mater. 2025, 8, 16053–16070

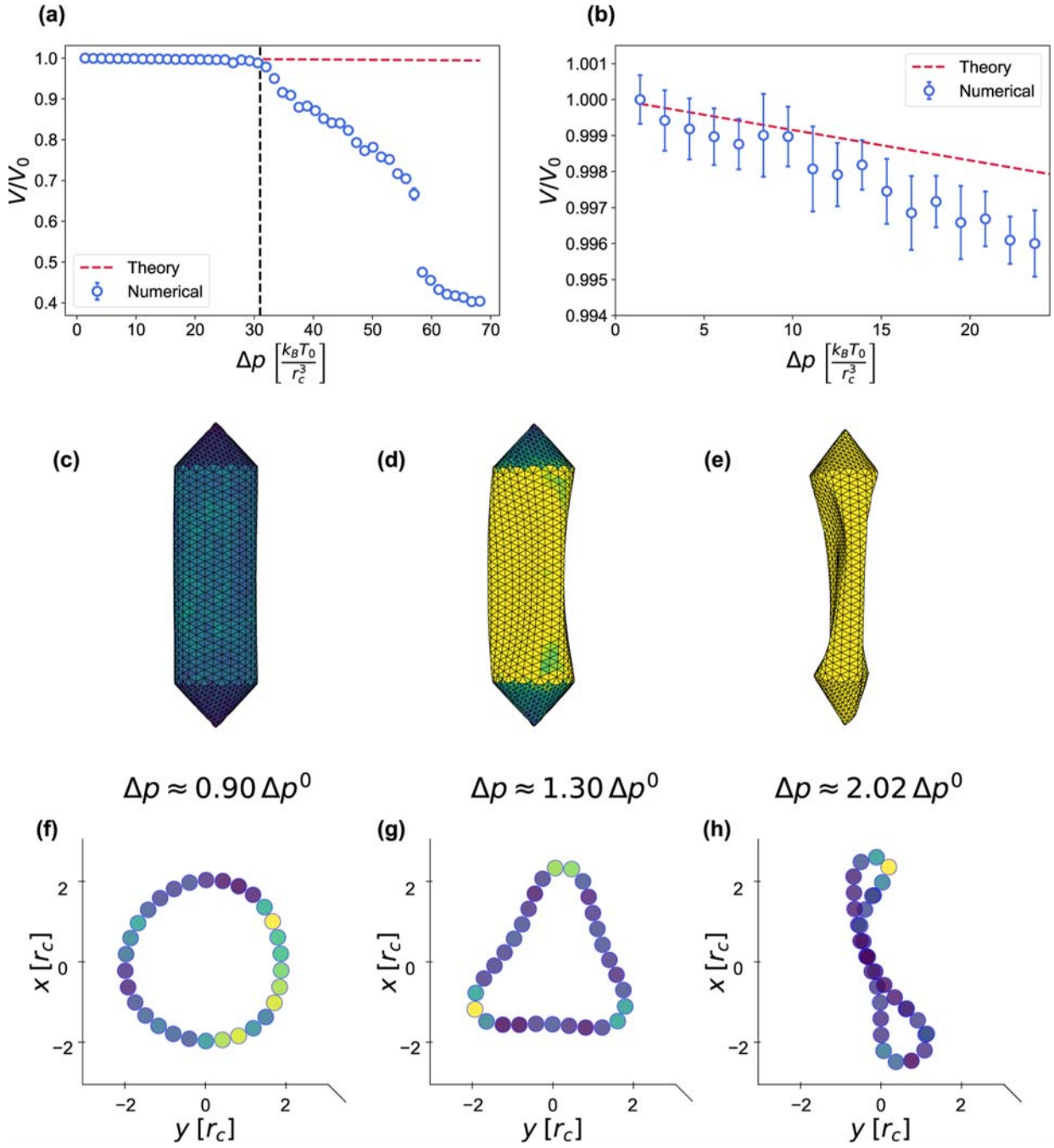

Figure 7. GV compression and buckling. (a) Relative volume change of a GV due to the external pressure increase Δp, compared to eq 27 (red dashed line). The buckling pressure $\Delta p^0 = 31.0\ k_B T_0/r_c^3$ is indicated by a black dashed vertical line. (b) Closeup of (a) in the small deformation regime. (c–e) Side views and (f–h) central transverse slices of the GV at different Δp. The coloring represents local elastic energy.

solutions to the linearized equations (Donnel theory[137]) of simply supported cylindrical shell (shear diaphragm at both ends at $z = -\frac{1}{2}H^0_{\mathrm{cyl}}$ and $z = \frac{1}{2}H^0_{\mathrm{cyl}}$),[138] $\mathbf{u}(z, \varphi, t) = (u_r\hat{\mathbf{e}}_r + u_\varphi\hat{\mathbf{e}}_\varphi + u_z\hat{\mathbf{e}}_z)\cos(\omega t)$, with

$$u_r = C_r \sin\left(\lambda_m z + \frac{m\pi}{2}\right)\cos(n\varphi) \tag{28}$$

$$u_\varphi = C_\varphi \sin\left(\lambda_m z + \frac{m\pi}{2}\right)\sin(n\varphi) \tag{29}$$

$$u_z = C_z \cos\left(\lambda_m z + \frac{m\pi}{2}\right)\cos(n\varphi) \tag{30}$$

where u_r, u_φ, u_z are displacement fields of the cylindrical shell in r, φ, and z directions, $\lambda_m = \frac{m\pi}{H^0_{\mathrm{cyl}}}$, and C_r, C_φ, C_z are the amplitudes, which depend on n, m, and the elastic coefficients.[138] For every mode with $n \neq 0$, there exists another mode with the same frequency, rotated by $\frac{\pi}{2n}$ around the z axis, i.e., with $\cos(n\varphi)$ and $\sin(n\varphi)$ in eqs 28–30 interchanged.

https://doi.org/10.1021/acsanm.5c02783
ACS Appl. Nano Mater. 2025, 8, 16053–16070

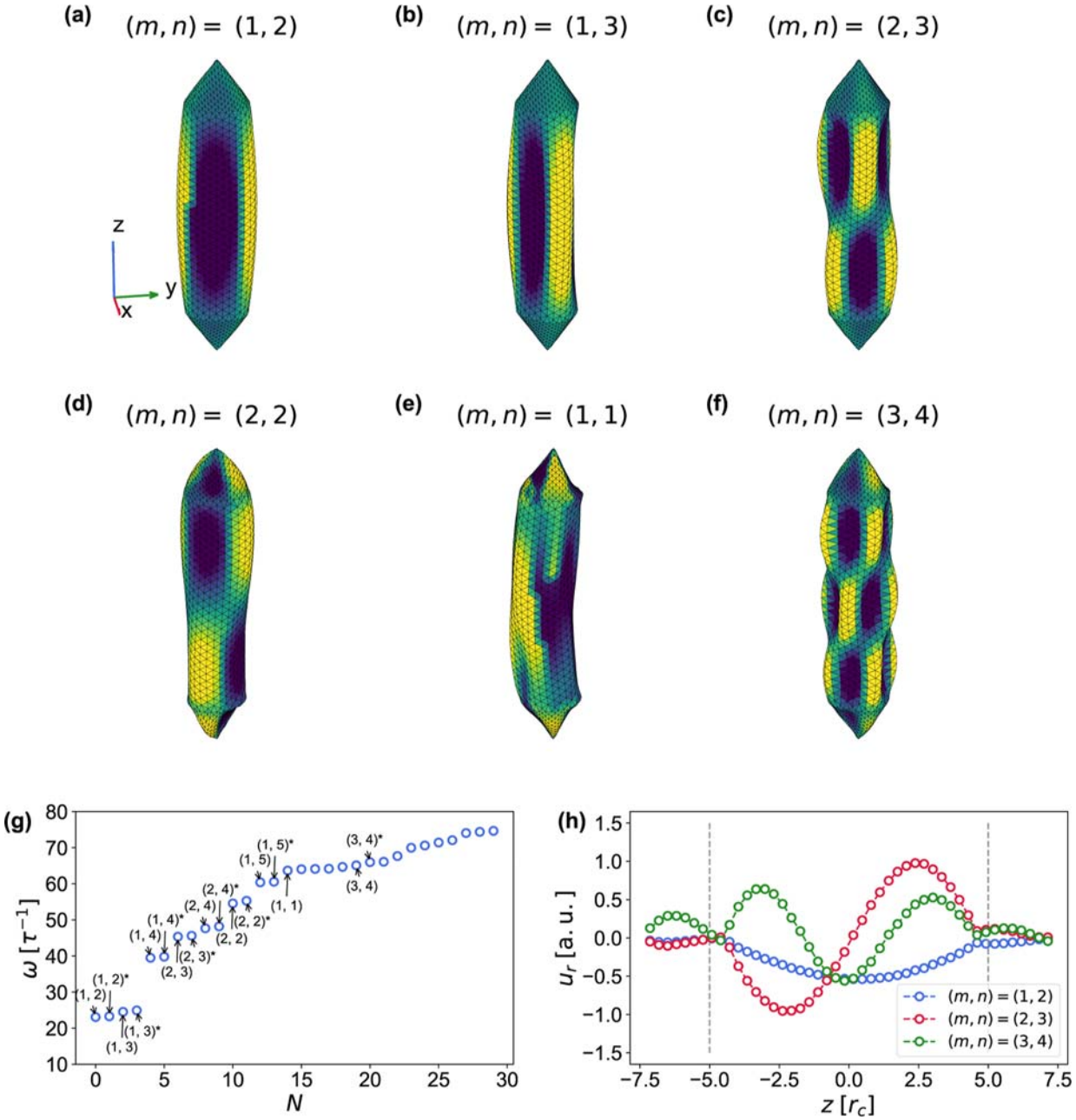

Figure 8. GV vibrational modes. (a–f) Selected low-frequency eigenmodes of a GV with corresponding axial and circumferential numbers m, n, ordered by increasing frequency. The mesh triangles are colored according to modal displacement. (g) First 30 eigenfrequencies with selected modes labeled by their mode indices (m, n). The star $(m,n)^*$ denotes an eigenmode rotated by $\frac{\pi}{2n}$ around the z axis, relative to the mode with the same indices (m, n). (h) The $u_r(z)$ profile (axial profile) of selected modes. The dashed lines indicate the ends of the GV cylinder.

The lowest-frequency mode is the doubly degenerate $(m, n) = (1, 2)$ mode, Figure 8a, with $\omega \approx 23.1\ \tau^{-1}$, corresponding to frequency $\nu \approx 201$ MHz. It resembles the GV shape at the second buckling transition, Figure 7e,h.

Our results can be compared with the FEM simulations of GVs in ref 65, where the lowest-frequency vibrational mode is the $(m, n) = (1, 1)$ mode at $\nu = 328$ MHz. The lower frequency in our case is due to the larger diameter of GV, 140 nm, compared to 85 nm in ref 65. Interestingly, in our case, the $(m, n) = (1, 1)$ mode appears only as the 15th mode in Figure 8g, with a frequency of $\nu \approx 555$ MHz.

The elastic shell dynamics that govern these low vibrational modes largely depend on the shell's elastic parameters, which are independent of the chosen DPD scale. Our chosen time step of $\Delta t = 10^{-4}\ \tau \approx 6.5$ ps is sufficient to resolve frequencies above 10 GHz, well beyond the ultrasound-relevant regime shown in Figure 8g. While our focus is on low-frequency behavior, capturing higher-frequency responses may require smaller scales[139,140] or coupling with atomistic models.[141]

3.11. Rheological Properties: Behavior in Shear Flow.

Considering the effects of shear forces on GV dynamics is crucial for their use in targeted drug delivery within the bloodstream. Since GVs are elongated and exhibit a wide range

https://doi.org/10.1021/acsanm.5c02783
ACS Appl. Nano Mater. 2025, 8, 16053−16070

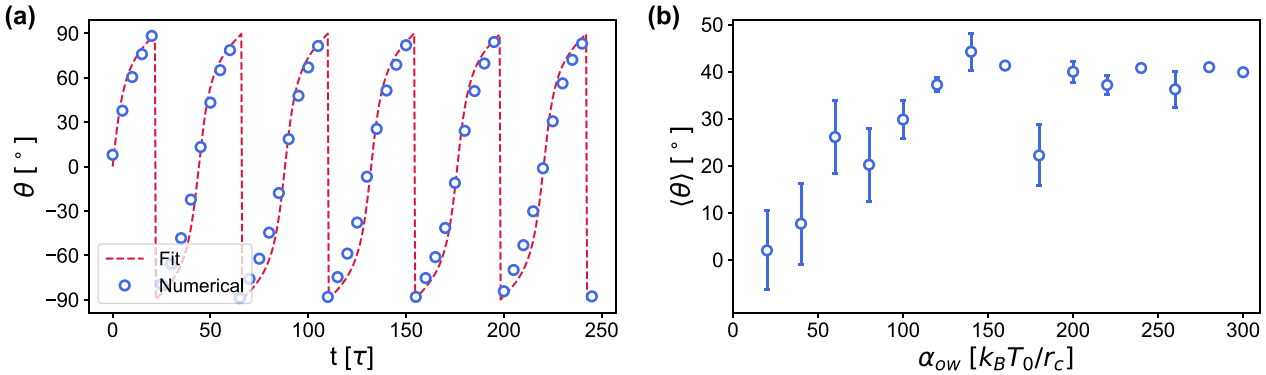

Figure 9. Tumbling and alignment of a GV in shear flow. (a) Time dependence of the GV axis inclination angle θ with respect to the flow direction for GV−water repulsion strength $a_{ow} = 50\ k_BT_0/r_c$ and GV−water dissipative interaction strength $\gamma_{ow} = 40\ m/\tau$ for $\dot{\gamma} = 0.0862\tau^{-1}$. Numerical values (blue circles) are compared to eq 31 (red dashed line). (b) Dependence of mean θ on a_{ow} for $\dot{\gamma} = 0.0862\tau^{-1}$.

of aspect ratios, their behavior in shear flow can be compared to that of ellipsoids. In shear flow, neutrally buoyant ellipsoids with no-slip boundary conditions undergo rotations known as Jeffery orbits.[142] During these rotations, the ellipsoid is continuously flipping in the shear plane (the plane spanned by the velocity and its gradient), and the angle θ between its axis and the velocity evolves as

$$\tan(\theta) = \frac{a}{b}\tan\left(\frac{ab\dot{\gamma}t}{a^2 + b^2}\right) \tag{31}$$

where a and b are the major and minor axes of the ellipsoid and $\dot{\gamma}$ is the shear rate.

Using OBMD, we generate shear flow and apply it to a GV fixed at the center of the domain but free to rotate. In our model, the dissipative interaction between the GV vertex beads and water beads, taking into account eq 9, ensures no-slip boundary condition. This boundary condition leads to a tumbling motion consistent with eq 31, as shown in Figure 9a. In principle, one could functionalize GVs with a hydrophobic surfactant. In such a case, the no-slip boundary condition may no longer apply, potentially altering the qualitative behavior of GVs in shear flow. To investigate this, we explore the GV response in shear flow depending on the repulsive interaction strength a_{ow} between the vertices and water beads.

The dependence of the mean inclination angle $\langle\theta\rangle$ on a_{ow} is shown in Figure 9b. The mean angle and its standard deviation were calculated over the second half of each simulation. For $0 < a_{ow} < 50\ k_BT_0/r_c$, the GV exhibits tumbling behavior. Above $a_{ow} \approx 50\ k_BT_0/r_c$, the GV aligns at a fixed angle in the shear plane, which increases to approximately 40° in the limit of large a_{ow}. Here, γ_{ow} was fixed to the value required by eq 9, which guarantees no-slip boundary conditions for $a_{ow} = 0$.

4. CONCLUSIONS

The growing demand for encapsulated materials in theranostic ultrasound applications underscores the need for versatile and robust modeling approaches. Current theoretical frameworks often rely on oversimplified descriptions, while fully atomistic models, though detailed, are computationally prohibitive for large-scale or dynamic simulations. In this paper, we developed a general framework for modeling shelled biomaterials, and presented particle-based mesoscopic models of EMBs and GVs as two representative applications. The elastic energy of their membrane was derived from the continuum theory of elasticity and discretized on a triangular surface, where we drew inspiration from RBC membrane network models. Thus, our description of membrane elasticity builds on the same theoretical foundation as existing force fields and compatibly encompasses previous models, e.g. for RBCs[91,116,143−150] or viral capsid shells.[151,152] Moreover, it extends this established framework by incorporating anisotropic elasticity, enabling straightforward application to anisotropic membranes such as GVs, which exhibit orthotropic elasticity due to increased stiffness along the ridges of the GvpA protein.

The elasticity of computational shell models is governed by elastic coefficients, including Young's moduli, Poisson's ratios, bending constants, as well as coefficients of mutual influence, which describe the coupling between extensional and shear strains, and Chentsov coefficients, which characterize the interaction of shear strains across different planes. These coefficients can be determined experimentally. Consequently, any membrane composition can be modeled by our framework, as long as its elastic properties are known. This has important implications for fields such as bioengineering and medical applications where elastic properties are concerned, as our framework can model a wide range of membrane-based systems of arbitrary shapes and local anisotropy, from biological cells to artificial capsules.

We validated the framework by simulating stretching, buckling, and shear flow dynamics of EMBs and GVs, comparing our results with theoretical predictions in the limit of small deformations. The stress−strain curves obtained from the stretching experiments agree well with the theory of linear deformation for both EMBs and GVs. Furthermore, we were able to reproduce the relationship between the critical buckling pressure and the membrane radius. We also derived analytical expressions that can be used for the experimental determination of the elastic coefficients.

However, the mechanical properties of fluid-immersed objects depend not only on the material of the membrane but also on their environment and the interactions with it. These interactions significantly influence the rheological behavior, which is crucial when modeling membranes in flow. In this study, we focused on simplified, controlled environments to isolate the intrinsic mechanical response of GVs and EMBs, modeling the surrounding medium as a simple Newtonian fluid within the DPD framework. However, we acknowledge that physiological viscoelastic intracellular conditions can significantly influence the dynamic behavior. Future extensions of the model could incorporate these effects to

https://doi.org/10.1021/acsanm.5c02783
ACS Appl. Nano Mater. 2025, 8, 16053−16070

enhance physiological relevance in gene delivery or imaging scenarios. DPD allows tuning of fluid−object interactions, thereby influencing the dynamic coupling between objects and the fluid. Proper adjustment of the dissipative parameter γ_{ow} enables control over the degree of slip in the boundary condition at the membrane−solvent interface, ranging from no-slip to full slip. Our shear flow numerical experiments demonstrated the rotational periodic motion (flow tumbling) of a single GV suspended in a DPD solvent, consistent with Jeffery's theoretical predictions. Moreover, we find that both the repulsion and dissipative parameters, a_{ow} and γ_{ow}, play a crucial role in GV motion, either inducing flow tumbling or leading to flow alignment at a specific inclination angle. This tunability of slip conditions also enables our model to account for physiologically relevant surface modifications, such as lipoprotein adsorption or surfactant functionalization, which may alter interfacial dynamics and influence particle behavior in vivo. While a detailed treatment of membrane functionalization is beyond the scope of this study, our framework is well-suited for future investigations of such effects, offering a path to model vesicle−fluid interactions under more complex biological conditions.

Interaction of ultrasound with encapsulated biomembranes is a highly relevant yet complex topic. While the current work focuses on the mechanical behavior of encapsulated structures under quasi-static conditions, modeling their dynamic response to propagating or standing-wave ultrasound fields is a central objective of our ongoing research. In typical biomedical ultrasound applications (100 kPa−1 MPa, 1−100 MHz), the applied pressures and frequencies are sufficient to induce both linear and nonlinear deformations of UCAs, including buckling and collapse, as supported by our results in Figure 6a and Figure 7a. Given that the wavelength of low-frequency ultrasound (10 μm−1 cm) greatly exceeds the characteristic size of the particles (100 nm−1 μm), such wavefields can be reasonably approximated as spatially uniform pressure loads at the particle scale. This approximation justifies the use of isotropic loading in our present simulations as a first-order model of therapeutic ultrasound exposure. Looking ahead, we plan to extend our framework using reactive dissipative particle dynamics (DPD-RX) to explicitly capture ultrasound-driven effects such as bond breakage, shell rupture, and gas exchange under high strain rates. This will allow us to model cavitation-like phenomena and shell failure, ultimately enabling more accurate simulation of therapeutic ultrasound scenarios.

While continuum models focus on modeling the dynamics of individual bubbles to elucidate fundamental principles,[60] our DPD approach extends beyond these limitations by allowing the simulation of multiple interacting bodies, thus capturing collective behavior and complex interactions that are critical in many applications. The presented modeling framework is a first step toward large-scale simulations of multiple micro- and nanostructures and their interaction with propagating ultrasound waves. Modeling the ultrasound propagation on mesoscopic scales with our virtual US machine[139,140,153,154] will assist and advance simulation-driven optimization of ultrasound-based theranostics. The optimal parameters that reproduce the given experiments can be efficiently determined using Bayesian uncertainty quantification.[91,118] The proposed computational framework would allow for controlled testing, data-driven quantification of uncertainties, and rational optimization of experimental US parameters.

■ ASSOCIATED CONTENT

Supporting Information

The Supporting Information is available free of charge at https://pubs.acs.org/doi/10.1021/acsanm.5c02783.

Elastic energy of EMBs and GVs with the corresponding nodal forces, numerical validation of the mechanical properties of a rectangular sheet, analytical expressions for the elastic behavior of EMBs and GVs in the limit of low strain, dependence of the microbubble buckling pressure on its radius, overview of the dissipative particle dynamics (DPD) and simulation details. (PDF)

■ AUTHOR INFORMATION

Corresponding Author

Matej Praprotnik − *Laboratory for Molecular Modeling, National Institute of Chemistry, SI-1001 Ljubljana, Slovenia; Department of Physics, Faculty of Mathematics and Physics, University of Ljubljana, SI-1000 Ljubljana, Slovenia; Universitat de Barcelona Institute of Complex Systems, 08028 Barcelona, Spain;* orcid.org/0000-0003-0825-1659; Email: praprot@cmm.ki.si

Authors

Nikolaos Ntarakas − *Laboratory for Molecular Modeling, National Institute of Chemistry, SI-1001 Ljubljana, Slovenia; Department of Physics, Faculty of Mathematics and Physics, University of Ljubljana, SI-1000 Ljubljana, Slovenia;* orcid.org/0000-0002-5137-8009

Maša Lah − *Laboratory for Molecular Modeling, National Institute of Chemistry, SI-1001 Ljubljana, Slovenia; Department of Physics, Faculty of Mathematics and Physics, University of Ljubljana, SI-1000 Ljubljana, Slovenia*

Daniel Svenšek − *Laboratory for Molecular Modeling, National Institute of Chemistry, SI-1001 Ljubljana, Slovenia; Department of Physics, Faculty of Mathematics and Physics, University of Ljubljana, SI-1000 Ljubljana, Slovenia*

Tilen Potisk − *Laboratory for Molecular Modeling, National Institute of Chemistry, SI-1001 Ljubljana, Slovenia; Department of Physics, Faculty of Mathematics and Physics, University of Ljubljana, SI-1000 Ljubljana, Slovenia;* orcid.org/0000-0002-8466-8993

Complete contact information is available at: https://pubs.acs.org/10.1021/acsanm.5c02783

Author Contributions

N.N., M.L. and T.P. performed the simulations. N.N., M.L., D.S., T.P. and M.P. analyzed the results and wrote the paper. N.N., M.L. and T.P. modified the software. M.P. acquired the funding and conceived the study.

Notes

The authors declare no competing financial interest.

■ ACKNOWLEDGMENTS

The authors acknowledge financial support under the ERC Advanced Grant MULTraSonicA (Grant No. 885155) from the European Research Council. The authors also acknowledge the financial support from the Slovenian Research and Innovation Agency (Grant No. P1-0002). Finally, the authors acknowledge the HPC RIVR consortium (www.hpc-rivr.si) and EuroHPC JU (eurohpc-ju.europa.eu) for providing computing resources of the HPC system Vega at the Institute of Information Science (www.izum.si).

REFERENCES

(1) Lee, H.; Kim, H.; Han, H.; Lee, M.; Lee, S.; Yoo, H.; Chang, J. H.; Kim, H. Microbubbles Used for Contrast Enhanced Ultrasound and Theragnosis: A Review of Principles to Applications. *Biomed. Eng. Lett.* **2017**, *7*, 59−69.

(2) Lindner, J. R. Microbubbles in Medical Imaging: Current Applications and Future Directions. *Nat. Rev. Drug Discovery* **2004**, *3*, 527.

(3) Schroeder, A.; Kost, J.; Barenholz, Y. Ultrasound, Liposomes, and Drug Delivery: Principles for Using Ultrasound to Control the Release of Drugs from Liposomes. *Chem. Phys. Lipids* **2009**, *162*, 1−16.

(4) Macé, E.; Montaldo, G.; Cohen, I.; Baulac, M.; Fink, M.; Tanter, M. Functional Ultrasound Imaging of the Brain. *Nat. Methods* **2011**, *8*, 662−664.

(5) Tanter, M.; Fink, M. Ultrafast Imaging in Biomedical Ultrasound. *IEEE Trans. Sonics Ultrason.* **2014**, *61*, 102−119.

(6) Rungta, R. L.; Osmanski, B. F.; Boido, D.; Tanter, M.; Charpak, S. Light Controls Cerebral Blood Flow in Naive Animals. *Nat. Commun.* **2017**, *8*, 14191.

(7) Mo, S.; Coussios, C.; Seymour, L.; Carlisle, R. Ultrasound-enhanced drug delivery for cancer. *Expert Opin. Drug Delivery* **2012**, *9*, 1525−1538.

(8) Wu, D.; Baresch, D.; Cook, C.; Ma, Z.; Duan, M.; Malounda, D.; Maresca, D.; Abundo, M. P.; Lee, J.; Shivaei, S.; et al. Biomolecular actuators for genetically selective acoustic manipulation of cells. *Sci. Adv.* **2023**, *9*, No. eadd9186.

(9) Zhou, Y.; Ye, M.; Hu, C.; Qian, H.; Nelson, B.; Wang, X. Stimuli-responsive functional micro-/nanorobots: a review. *ACS Nano* **2023**, *17*, 15254−15276.

(10) Zhang, H.; Tang, J.; Cao, H.; Wang, C.; Shen, C.; Liu, J. Review of the applications of micro/nanorobots in biomedicine. *ACS Appl. Nano Mater.* **2024**, *7*, 17151−17192.

(11) Paul, S.; Nahire, R.; Mallik, S.; Sarkar, K. Encapsulated microbubbles and echogenic liposomes for contrast ultrasound imaging and targeted drug delivery. *Comput. Mech.* **2014**, *53*, 413−435.

(12) Wang, T.-Y.; Wilson, K. E.; Machtaler, S.; Willmann, J. K. Ultrasound and Microbubble Guided Drug Delivery: Mechanistic Understanding and Clinical Implications. *Curr. Pharm. Biotechnol.* **2014**, *14*, 743−752.

(13) Unger, E.; Porter, T.; Lindner, J.; Grayburn, P. Cardiovascular drug delivery with ultrasound and microbubbles. *Adv. Drug Delivery Rev.* **2014**, *72*, 110−126.

(14) Meng, L.; Liu, X.; Wang, Y.; Zhang, W.; Zhou, W.; Cai, F.; Li, F.; Wu, J.; Xu, L.; Niu, L.; et al. Sonoporation of cells by a parallel stable cavitation microbubble array. *Adv. Sci.* **2019**, *6*, 1900557.

(15) Choi, J. J.; Feshitan, J. A.; Baseri, B.; Wang, S.; Tung, Y.-S.; Borden, M. A.; Konofagou, E. E. Microbubble-size dependence of focused ultrasound-induced blood−brain barrier opening in mice in vivo. *IEEE Trans. Biomed. Eng.* **2010**, *57*, 145−154.

(16) Choi, J. J.; Selert, K.; Vlachos, F.; Wong, A.; Konofagou, E. E. Noninvasive and localized neuronal delivery using short ultrasonic pulses and microbubbles. *Proc. Natl. Acad. Sci. U.S.A.* **2011**, *108*, 16539−16544.

(17) Konofagou, E. E. Optimization of the ultrasound-induced blood-brain barrier opening. *Theranostics* **2012**, *2*, 1223.

(18) Ferrara, K.; Pollard, R.; Borden, M. Ultrasound microbubble contrast agents: fundamentals and application to gene and drug delivery. *Annu. Rev. Biomed. Eng.* **2007**, *9*, 415−447.

(19) Lakshmanan, A.; Farhadi, A.; Nety, S. P.; Lee-Gosselin, A.; Bourdeau, R. W.; Maresca, D.; Shapiro, M. G. Molecular Engineering of Acoustic Protein Nanostructures. *ACS Nano* **2016**, *10*, 7314−7322.

(20) Maresca, D.; Lakshmanan, A.; Lee-Gosselin, A.; Melis, J. M.; Ni, Y.-L.; Bourdeau, R. W.; Kochmann, D. M.; Shapiro, M. G. Nonlinear Ultrasound Imaging of Nanoscale Acoustic Biomolecules. *Appl. Phys. Lett.* **2017**, *110*, 073704.

(21) Main, M. L.; Hibberd, M. G.; Ryan, A.; Lowe, T. J.; Miller, P.; Bhat, G. Acute mortality in critically ill patients undergoing echocardiography with or without an ultrasound contrast agent. *JACC: Cardiovasc. Imaging* **2014**, *7*, 40−48.

(22) Sirsi, S.; Borden, M. Microbubble compositions, properties and biomedical applications. *Bubble Sci., Eng., Technol.* **2009**, *1*, 3−17.

(23) Choi, J.; Coussios, C. Spatiotemporal evolution of cavitation dynamics exhibited by flowing microbubbles during ultrasound exposure. *J. Acoust. Soc. Am.* **2012**, *132*, 3538−3549.

(24) Coussios, C.; Roy, R. Applications of acoustics and cavitation to noninvasive therapy and drug delivery. *Annu. Rev. Fluid. Mech.* **2008**, *40*, 395−420.

(25) Pandur, Ž.; Zevnik, J.; Podbevšek, D.; Stojković, B.; Stopar, D.; Dular, M. Water treatment by cavitation: Understanding it at a single bubble-bacterial cell level. *Water Res.* **2023**, *236*, 119956.

(26) Ezzeldin, H. M.; Klauda, J. B.; Solares, S. D. Modeling of the Major Gas Vesicle Protein, GvpA: From Protein Sequence to Vesicle Wall Structure. *J. Struct. Biol.* **2012**, *179*, 18−28.

(27) Park, J.; Kim, K. W. Microscopy of Microbial Gas Vesicles. *Appl. Microsc.* **2017**, *47*, 165−170.

(28) Walsby, A. E. Structure and Function of Gas Vacuoles. *Bacteriol. Rev.* **1972**, *36*, 1−32.

(29) Walsby, A. E. Gas Vesicles. *Microbiol. Rev.* **1994**, *58*, 94−144.

(30) Walsby, A. E.; Fogg, G. E. The Pressure Relationships of Gas Vacuoles. *Proc. R. Soc. London, Ser. B* **1971**, *178*, 301−326.

(31) Xu, B.-Y.; Dai, Y.-N.; Zhou, K.; Liu, Y.-T.; Sun, Q.; Ren, Y.-M.; Chen, Y.; Zhou, C.-Z. Structure of the Gas Vesicle Protein GvpF from the Cyanobacterium Microcystis Aeruginosa. *Acta Crystallogr., Sect. D: Biol. Crystallogr.* **2014**, *70*, 3013−3022.

(32) Yang, Y.; Qiu, Z.; Hou, X.; Sun, L. Ultrasonic Characteristics and Cellular Properties of Anabaena Gas Vesicles. *Ultrasound Med. Biol.* **2017**, *43*, 2862−2870.

(33) Jazbec, V.; Varda, N.; Šprager, E.; Meško, M.; Vidmar, S.; Romih, R.; Podobnik, M.; Kežar, A.; Jerala, R.; Benčina, M. Protein Gas Vesicles of Bacillus megaterium as Enhancers of Ultrasound-Induced Transcriptional Regulation. *ACS Nano* **2024**, *18*, 16692−16700.

(34) Dutka, P.; Metskas, L. A.; Hurt, R. C.; Salahshoor, H.; Wang, T.-Y.; Malounda, D.; Lu, G. J.; Chou, T.-F.; Shapiro, M. G.; Jensen, G. J. Structure of Anabaena flos-aquae gas vesicles revealed by cryo-ET. *Structure* **2023**, *31*, 518−528.

(35) Huber, S. T.; Terwiel, D.; Evers, W. H.; Maresca, D.; Jakobi, A. J. Cryo-EM structure of gas vesicles for buoyancy-controlled motility. *Cell* **2023**, *186*, 975−986 e13.

(36) Offner, S.; Ziese, U.; Wanner, G.; Typke, D.; Pfeifer, F. Structural characteristics of halobacterial gas vesicles. *Microbiology* **1998**, *144*, 1331−1342.

(37) Maresca, D.; Lakshmanan, A.; Abedi, M.; Bar-Zion, A.; Farhadi, A.; Lu, G. J.; Szablowski, J. O.; Wu, D.; Yoo, S.; Shapiro, M. G. Biomolecular Ultrasound and Sonogenetics. *Annu. Rev. Chem. Biomol. Eng.* **2018**, *9*, 229−252.

(38) De Jong, N.; Bouakaz, A.; Frinking, P. Basic Acoustic Properties of Microbubbles. *Echocardiography* **2002**, *19*, 229−240.

(39) Sboros, V. Response of contrast agents to ultrasound. *Adv. Drug Delivery Rev.* **2008**, *60*, 1117−1136.

(40) Noguchi, H.; Gompper, G. Shape Transitions of Fluid Vesicles and Red Blood Cells in Capillary Flows. *Proc. Natl. Acad. Sci. U.S.A.* **2005**, *102*, 14159−14164.

(41) Dupin, M. M.; Halliday, I.; Care, C. M.; Alboul, L.; Munn, L. L. Modeling the Flow of Dense Suspensions of Deformable Particles in Three Dimensions. *Phys. Rev. E* **2007**, *75*, 066707.

(42) Discher, D. E.; Boal, D. H.; Boey, S. K. Simulations of the Erythrocyte Cytoskeleton at Large Deformation. II. Micropipette Aspiration. *Biophys. J.* **1998**, *75*, 1584−1597.

(43) Li, J.; Dao, M.; Lim, C. T.; Suresh, S. Spectrin-Level Modeling of the Cytoskeleton and Optical Tweezers Stretching of the Erythrocyte. *Biophys. J.* **2005**, *88*, 3707−3719.

(44) Pivkin, I. V.; Karniadakis, G. E. Accurate Coarse-Grained Modeling of Red Blood Cells. *Phys. Rev. Lett.* **2008**, *101*, 118105.

https://doi.org/10.1021/acsanm.5c02783
ACS Appl. Nano Mater. 2025, 8, 16053−16070

(45) Gompper, G.; Kroll, D. M. Network Models of Fluid, Hexatic and Polymerized Membranes. *J. Phys.: Condens. Matter* **1997**, *9*, 8795−8834.
(46) Gompper, G.; Kroll, D. Triangulated-surface models of fluctuating membranes. In *Statistical Mechanics of Membranes and Surfaces*; World Scientific, 2004; pp 359−426.
(47) Noguchi, H.; Gompper, G. Dynamics of Fluid Vesicles in Shear Flow: Effect of Membrane Viscosity and Thermal Fluctuations. *Phys. Rev. E* **2005**, *72*, 011901.
(48) Fedosov, D. A.; Caswell, B.; Karniadakis, G. E. A Multiscale Red Blood Cell Model with Accurate Mechanics, Rheology, and Dynamics. *Biophys. J.* **2010**, *98*, 2215−2225.
(49) Fedosov, D. A.; Caswell, B.; Karniadakis, G. E. Systematic Coarse-Graining of Spectrin-Level Red Blood Cell Models. *Comput. Meth. Appl. Mech. Eng.* **2010**, *199*, 1937−1948.
(50) Fedosov, D. A.; Lei, H.; Caswell, B.; Suresh, S.; Karniadakis, G. E. Multiscale Modeling of Red Blood Cell Mechanics and Blood Flow in Malaria. *PLoS Comput. Biol.* **2011**, *7*, No. e1002270.
(51) Fedosov, D. A.; Peltomäki, M.; Gompper, G. Deformation and Dynamics of Red Blood Cells in Flow through Cylindrical Microchannels. *Soft Matter* **2014**, *10*, 4258−4267.
(52) Müller, K.; Fedosov, D. A.; Gompper, G. Understanding Particle Margination in Blood Flow − A Step toward Optimized Drug Delivery Systems. *Med. Eng. Phys.* **2016**, *38*, 2−10.
(53) Shi, X.; Lin, G.; Zou, J.; Fedosov, D. A. A Lattice Boltzmann Fictitious Domain Method for Modeling Red Blood Cell Deformation and Multiple-Cell Hydrodynamic Interactions in Flow. *Int. J. Numer. Methods Fluids* **2013**, *72*, 895−911.
(54) Ye, T.; Phan-Thien, N.; Khoo, B. C.; Lim, C. T. Dissipative Particle Dynamics Simulations of Deformation and Aggregation of Healthy and Diseased Red Blood Cells in a Tube Flow. *Phys. Fluids* **2014**, *26*, 111902.
(55) Ye, T.; Phan-Thien, N.; Khoo, B. C.; Lim, C. T. A File of Red Blood Cells in Tube Flow: A Three-Dimensional Numerical Study. *J. Appl. Phys.* **2014**, *116*, 124703.
(56) Rossinelli, D.; Hejazialhosseini, B.; Hadjidoukas, P.; Bekas, C.; Curioni, A.; Bertsch, A.; Futral, S.; Schmidt, S. J.; Adams, N. A.; Koumoutsakos, P. 11 PFLOP/s simulations of cloud cavitation collapse. In *Proceedings of the International Conference on High Performance Computing, Networking, Storage and Analysis*, 2013, pp 1−13.
(57) Rasthofer, U.; Wermelinger, F.; Karnakov, P.; Šukys, J.; Koumoutsakos, P. Computational study of the collapse of a cloud with 12500 gas bubbles in a liquid. *Phys. Rev. Fluids* **2019**, *4*, 063602.
(58) Rayleigh, L. V. I. I. I. VIII. *On the pressure developed in a liquid during the collapse of a spherical cavity*. *Philos. Mag. J. Sci.* **1917**, *34*, 94−98.
(59) Hickling, R.; Plesset, M. S. Collapse and Rebound of a Spherical Bubble in Water. *Phys. Fluids* **1964**, *7*, 7−14.
(60) Dollet, B.; Marmottant, P.; Garbin, V. Bubble Dynamics in Soft and Biological Matter. *Annu. Rev. Fluid. Mech.* **2019**, *51*, 331−355.
(61) Medwin, H. Counting Bubbles Acoustically: A Review. *Ultrasonics* **1977**, *15*, 7−13.
(62) Qin, S.; Caskey, C. F.; Ferrara, K. W. Ultrasound Contrast Microbubbles in Imaging and Therapy: Physical Principles and Engineering. *Phys. Med. Biol.* **2009**, *54*, R27−R57.
(63) Nawijn, C.; Spiekhout, S.; Voorneveld, J.; Bosch, J.; Versluis, M.; Segers, T.; Lajoinie, G. Stress-strain analysis of single ultrasound-driven microbubbles for viscoelastic shell characterization. *J. Acoust. Soc. Am.* **2025**, *157*, 897−911.
(64) Zhang, S.; Huang, A.; Bar-Zion, A.; Wang, J.; Mena, O. V.; Shapiro, M. G.; Friend, J. The vibration behavior of sub-micrometer gas vesicles in response to acoustic excitation determined via laser doppler vibrometry. *Adv. Funct. Mater.* **2020**, *30*, 2000239.
(65) Salahshoor, H.; Yao, Y.; Dutka, P.; Nyström, N. N.; Jin, Z.; Min, E.; Malounda, D.; Jensen, G. J.; Ortiz, M.; Shapiro, M. G. Geometric effects in gas vesicle buckling under ultrasound. *Biophys. J.* **2022**, *121*, 4221−4228.
(66) Cherin, E.; Melis, J. M.; Bourdeau, R. W.; Yin, M.; Kochmann, D. M.; Foster, F. S.; Shapiro, M. G. Acoustic Behavior of Halobacterium Salinarum Gas Vesicles in the High-Frequency Range: Experiments and Modeling. *Ultrasound Med. Biol.* **2017**, *43*, 1016−1030.
(67) Zhao, T. Y.; Dunbar, M.; Keten, S.; Patankar, N. A. The buckling-condensation mechanism driving gas vesicle collapse. *Soft Matter* **2023**, *19*, 1174−1185.
(68) Smith, C.; Bar-Zion, A.; Wu, Q.; Malounda, D.; Bau, L.; Stride, E.; Shapiro, M.; Coussios, C. Ultrafast optical and passive acoustic mapping characterization of nanoscale cavitation nuclei based on gas vesicle proteins. *AIP Adv.* **2025**, *15*, 025016.
(69) de Jong, N.; Hoff, L.; Skotland, T.; Bom, N. Absorption and Scatter of Encapsulated Gas Filled Microspheres: Theoretical Considerations and Some Measurements. *Ultrasonics* **1992**, *30*, 95−103.
(70) de Jong, N.; Cornet, R.; Lancée, C. T. Higher Harmonics of Vibrating Gas-Filled Microspheres. Part One: Simulations. *Ultrasonics* **1994**, *32*, 447−453.
(71) de Jong, N.; Cornet, R.; Lancée, C. T. Higher Harmonics of Vibrating Gas-Filled Microspheres. Part Two: Measurements. *Ultrasonics* **1994**, *32*, 455−459.
(72) Marmottant, P.; van der Meer, S.; Emmer, M.; Versluis, M.; de Jong, N.; Hilgenfeldt, S.; Lohse, D. A Model for Large Amplitude Oscillations of Coated Bubbles Accounting for Buckling and Rupture. *J. Acoust. Soc. Am.* **2005**, *118*, 3499−3505.
(73) Marmottant, P.; Biben, T.; Hilgenfeldt, S. Deformation and Rupture of Lipid Vesicles in the Strong Shear Flow Generated by Ultrasound-Driven Microbubbles. *Proc. R. Soc. A* **2008**, *464*, 1781−1800.
(74) Marmottant, P.; Bouakaz, A.; Jong, N. d.; Quilliet, C. Buckling Resistance of Solid Shell Bubbles under Ultrasound. *J. Acoust. Soc. Am.* **2011**, *129*, 1231−1239.
(75) Sassaroli, E.; Hynynen, K. Resonance Frequency of Microbubbles in Small Blood Vessels: A Numerical Study. *Phys. Med. Biol.* **2005**, *50*, 5293−5305.
(76) Hosseinkhah, N.; Hynynen, K. A Three-Dimensional Model of an Ultrasound Contrast Agent Gas Bubble and Its Mechanical Effects on Microvessels. *Phys. Med. Biol.* **2012**, *57*, 785−808.
(77) Hosseinkhah, N.; Goertz, D. E.; Hynynen, K. Microbubbles and Blood−Brain Barrier Opening: A Numerical Study on Acoustic Emissions and Wall Stress Predictions. *IEEE Trans. Biomed. Eng.* **2015**, *62*, 1293−1304.
(78) Alexeev, D.; Amoudruz, L.; Litvinov, S.; Koumoutsakos, P. Mirheo: high-performance mesoscale simulations for microfluidics. *Comput. Phys. Commun.* **2020**, *254*, 107298.
(79) Hoogerbrugge, P. J.; Koelman, J. M. V. A. Simulating Microscopic Hydrodynamic Phenomena with Dissipative Particle Dynamics. *Europhys. Lett.* **1992**, *19*, 155−160.
(80) Frenkel, D.; Smit, B. *Understanding Molecular Simulation: From Algorithms to Applications*; Elsevier, 2002.
(81) Smit, B.; Kranenburg, M.; Sperotto, M.; Venturoli, M. Mesoscopic simulations of biological membranes. *Computer Simulations in Condensed Matter Systems: From Materials to Chemical Biology*; Springer, 2006; Vol. 2, 259−286..
(82) Español, P. Hydrodynamics from Dissipative Particle Dynamics. *Phys. Rev. E* **1995**, *52*, 1734−1742.
(83) Groot, R. D.; Warren, P. B. Dissipative Particle Dynamics: Bridging the Gap between Atomistic and Mesoscopic Simulation. *J. Chem. Phys.* **1997**, *107*, 4423−4435.
(84) Marsh, C. A.; Backx, G.; Ernst, M. H. Static and Dynamic Properties of Dissipative Particle Dynamics. *Phys. Rev. E* **1997**, *56*, 1676−1691.
(85) Dzwinel, W.; Yuen, D. A. Matching macroscopic properties of binary fluids to the interactions of dissipative particle dynamics. *Int. J. Mod. Phys. C* **2000**, *11*, 1−25.
(86) Trofimov, S. Y. Thermodynamic Consistency in Dissipative Particle Dynamics. Ph.D. Thesis, Technische Universiteit Eindhoven, Eindhoven, The Netherlands, 2003.

https://doi.org/10.1021/acsanm.5c02783
ACS Appl. Nano Mater. 2025, 8, 16053−16070

(87) Pivkin, I. V.; Karniadakis, G. E. Coarse-graining limits in open and wall-bounded dissipative particle dynamics systems. *J. Chem. Phys.* **2006**, *124*, 184101.
(88) Wang, X.; Santo, K. P.; Neimark, A. V. Modeling Gas−Liquid Interfaces by Dissipative Particle Dynamics: Adsorption and Surface Tension of Cetyl Trimethyl Ammonium Bromide at the Air−Water Interface. *Langmuir* **2020**, *36*, 14686−14698.
(89) Santo, K. P.; Iepure, M.; Arrendondo, J.; Min, Y.; Neimark, A. V. Temperature-dependent mechanical and phase behavior of pulmonary surfactant monolayers studied by dissipative particle dynamics modeling and experiments. *Colloids Surf., A* **2025**, *725*, 137623.
(90) Paulose, J.; Vliegenthart, G. A.; Gompper, G.; Nelson, D. R. Fluctuating shells under pressure. *Proc. Natl. Acad. Sci. U.S.A.* **2012**, *109*, 19551−19556.
(91) Economides, A.; Arampatzis, G.; Alexeev, D.; Litvinov, S.; Amoudruz, L.; Kulakova, L.; Papadimitriou, C.; Koumoutsakos, P. Hierarchical Bayesian Uncertainty Quantification for a Model of the Red Blood Cell. *Phys. Rev. Appl.* **2021**, *15*, 034062.
(92) De Gennes, P. G. Wetting: statics and dynamics. *Rev. Mod. Phys.* **1985**, *57*, 827.
(93) Tsuji, Y.; Tanaka, T.; Ishida, T. Lagrangian numerical simulation of plug flow of cohesionless particles in a horizontal pipe. *Powder Technol.* **1992**, *71*, 239−250.
(94) Revenga, M.; Zúñiga, I.; Español, P. Boundary conditions in dissipative particle dynamics. *Comput. Phys. Commun.* **1999**, *121*, 309−311.
(95) Delgado-Buscalioni, R.; Sablić, J.; Praprotnik, M. Open boundary molecular dynamics. *Eur. Phys. J.: Spec. Top.* **2015**, *224*, 2331−2349.
(96) Delle Site, L.; Praprotnik, M. Molecular systems with open boundaries: Theory and simulation. *Phys. Rep.* **2017**, *693*, 1−56.
(97) Potisk, T.; Sablić, J.; Svenšek, D.; Diego, E. S.-d.; Teran, F. J.; Praprotnik, M. Analyte-Driven Clustering of Bio-Conjugated Magnetic Nanoparticles. *Adv. Theory Simul.* **2023**, *6*, 2200796.
(98) Delgado-Buscalioni, R.; Coveney, P. V. USHER: An algorithm for particle insertion in dense fluids. *J. Chem. Phys.* **2003**, *119*, 978−987.
(99) Karplus, M.; Kushick, J. N. Method for estimating the configurational entropy of macromolecules. *Macromolecules* **1981**, *14*, 325−332.
(100) Amadei, A.; Linssen, A. B. M.; Berendsen, H. J. C. Essential dynamics of proteins. *Proteins* **1993**, *17*, 412−425.
(101) Brooks, B. R.; Janežič, D.; Karplus, M. Harmonic analysis of large systems. I. Methodology. *J. Comput. Chem.* **1995**, *16*, 1522−1542.
(102) Hotelling, H. Analysis of a complex of statistical variables into principal components. *J. Educ. Psychol.* **1933**, *24*, 417.
(103) Xu, Z. P.; Zheng, Q. S.; Jiang, Q.; Ma, C. C.; Zhao, Y.; Chen, G. H.; Gao, H.; Ren, G. X. Trans-phonon effects in ultra-fast nanodevices. *Nanotechnology* **2008**, *19*, 255705.
(104) Chen, C.; Ma, M.; Jin, K.; Liu, J. Z.; Shen, L.; Zheng, Q.; Xu, Z. Nanoscale fluid-structure interaction: Flow resistance and energy transfer between water and carbon nanotubes. *Phys. Rev. E:Stat., Nonlinear, Soft Matter Phys.* **2011**, *84*, 046314.
(105) Michaud-Agrawal, N.; Denning, E. J.; Woolf, T. B.; Beckstein, O. MDAnalysis: a toolkit for the analysis of molecular dynamics simulations. *J. Comput. Chem.* **2011**, *32*, 2319−2327.
(106) Gowers, R. J.; Linke, M.; Barnoud, J.; Reddy, T. J. E.; Melo, M. N.; Seyler, S. L.; Domanski, J. J.; Dotson, D. L.; Buchoux, S.; Kenney, I. M.; Beckstein, O. MDAnalysis: A Python Package for the Rapid Analysis of Molecular Dynamics Simulations. In *Proceedings of the 15th Python in Science Conference*, 2016, pp 98−105.
(107) Theobald, D. L. Rapid calculation of RMSDs using a quaternion-based characteristic polynomial. *Acta Crystallogr., Sect. A* **2005**, *61*, 478−480.
(108) Liu, P.; Agrafiotis, D. K.; Theobald, D. L. Fast determination of the optimal rotational matrix for macromolecular superpositions. *J. Comput. Chem.* **2010**, *31*, 1561−1563.
(109) Ussing, H. H. Transport of ions across cellular membranes. *Physiol. Rev.* **1949**, *29*, 127−155.
(110) Pandit, S. A.; Scott, H. L. In *Soft Matter, Vol 4: Lipid Bilayers and Red Blood Cells*; Gompper, G., Schick, M., Eds.; Wiley VCH: Weinheim, 2008; pp 1−82.
(111) Seung, H. S.; Nelson, D. R. Defects in flexible membranes with crystalline order. *Phys. Rev. A* **1988**, *38*, 1005−1018.
(112) Lidmar, J.; Mirny, L.; Nelson, D. R. Virus shapes and buckling transitions in spherical shells. *Phys. Rev. E* **2003**, *68*, 051910.
(113) Bonet, J.; Wood, R. D. *Nonlinear Continuum Mechanics for Finite Element Analysis*; Cambridge University Press: Cambridge, 1997.
(114) Komura, S.; Tamura, K.; Kato, T. Buckling of spherical shells adhering onto a rigid substrate. *Eur. Phys. J. E* **2005**, *18*, 343−358.
(115) Turner, M. J.; Clough, R. W.; Martin, H. C.; Topp, L. Stiffness and deflection analysis of complex structures. *J. Aeronaut. Sci.* **1956**, *23*, 805−823.
(116) Fedosov, D. A.; Caswell, B.; Karniadakis, G. E. A multiscale red blood cell model with accurate mechanics, rheology, and dynamics. *Biophys. J.* **2010**, *98*, 2215−2225.
(117) Economides, A.; Amoudruz, L.; Litvinov, S.; Alexeev, D.; Nizzero, S.; Hadjidoukas, P. E.; Rossinelli, D.; Koumoutsakos, P. Towards the Virtual Rheometer: High Performance Computing for the Red Blood Cell Microstructure. In *Proceedings of the Platform for Advanced Scientific Computing Conference*, 2017, pp 1−13.
(118) Amoudruz, L.; Economides, A.; Arampatzis, G.; Koumoutsakos, P. The stress-free state of human erythrocytes: Data-driven inference of a transferable RBC model. *Biophys. J.* **2023**, *122*, 1517−1525.
(119) Liu, S. C.; Derick, L. H.; Palek, J. Visualization of the hexagonal lattice in the erythrocyte membrane skeleton. *J. Cell Biol.* **1987**, *104*, 527−536.
(120) Vlachomitrou, M.; Pelekasis, N. Dynamic simulation of a coated microbubble in an unbounded flow: response to a step change in pressure. *J. Fluid Mech.* **2017**, *822*, 717−761.
(121) Chabouh, G.; van Elburg, B.; Versluis, M.; Segers, T.; Quilliet, C.; Coupier, G. Buckling of lipidic ultrasound contrast agents under quasi-static load. *Philos. Trans. R. Soc., A* **2023**, *381*, 20220025.
(122) Lempriere, B. Poisson's ratio in orthotropic materials. *AIAA J.* **1968**, *6*, 2226−2227.
(123) Li, Y.; Barbic, J. Stable Orthotropic Materials. In *Symposium on Computer Animation*, 2014, pp 41−46.
(124) Spencer, A. J. M. *Continuum Theory of the Mechanics of Fibre-Reinforced Composites*; Springer Vienna, 1984; pp 1−32.
(125) Timoshenko, S.; Woinowsky-Krieger, S. *Theory of Plates and Shells*, 2nd ed.; McGraw Hill: New York, 1959.
(126) Dao, M.; Lim, C. T.; Suresh, S. Mechanics of the human red blood cell deformed by optical tweezers. *J. Mech. Phys. Solids* **2003**, *51*, 2259−2280.
(127) Rivlin, R. S.; Saunders, D. Large elastic deformations of isotropic materials VII. Experiments on the deformation of rubber. *Philos. Trans. R. Soc., A* **1951**, *243*, 251−288.
(128) Stammen, J. A.; Williams, S.; Ku, D. N.; Guldberg, R. E. Mechanical properties of a novel PVA hydrogel in shear and unconfined compression. *Biomaterials* **2001**, *22*, 799−806.
(129) Deufel, C.; Forth, S.; Simmons, C. R.; Dejgosha, S.; Wang, M. D. Nanofabricated quartz cylinders for angular trapping: DNA supercoiling torque detection. *Nat. Methods* **2007**, *4*, 223−225.
(130) Bai, L.; Fulbright, R. M.; Wang, M. D. Mechanochemical Kinetics of Transcription Elongation. *Phys. Rev. Lett.* **2007**, *98*, 068103.
(131) Hénon, S.; Lenormand, G.; Richert, A.; Gallet, F. A New Determination of the Shear Modulus of the Human Erythrocyte Membrane Using Optical Tweezers. *Biophys. J.* **1999**, *76*, 1145−1151.
(132) Walsby, A. E.; Fogg, G. E. The elastic compressibility of gas vesicles. In *Proceedings of the Royal Society of London. Series B. Biological Sciences*, 1982, pp 355−368.
(133) Newman, F.; Searle, V. *The General Properties of Matter*; Edward Arnold: London, 1957.

https://doi.org/10.1021/acsanm.5c02783
ACS Appl. Nano Mater. 2025, 8, 16053−16070

(134) Vliegenthart, G. A.; Gompper, G. Compression, crumpling and collapse of spherical shells and capsules. *New J. Phys.* **2011**, *13*, 045020.
(135) Bouakaz, A.; De Jong, N. Native tissue imaging at superharmonic frequencies. *IEEE Trans. Sonics Ultrason.* **2003**, *50*, 496−506.
(136) Zhang, Y.; Yu, J.; Bomba, H. N.; Zhu, Y.; Gu, Z. Mechanical force-triggered drug delivery. *Chem. Rev.* **2016**, *116*, 12536−12563.
(137) Donnell, L. H. A New Theory for the Buckling of Thin Cylinders Under Axial Compression and Bending. *J. Fluids Eng.* **1934**, *56*, 795−806.
(138) Amabili, M. *Nonlinear Mechanics of Shells and Plates in Composite, Soft and Biological Materials*; Cambridge University Press, 2018.
(139) Papež, P.; Praprotnik, M. Dissipative particle dynamics simulation of ultrasound propagation through liquid water. *J. Chem. Theory Comput.* **2022**, *18*, 1227−1240.
(140) Lah, M.; Ntarakas, N.; Potisk, T.; Papež, P.; Praprotnik, M. Open-boundary molecular dynamics of ultrasound using supra-molecular water models. *J. Chem. Phys.* **2025**, *162*, 024103.
(141) Praprotnik, M.; Delle Site, L.; Kremer, K. Adaptive resolution molecular-dynamics simulation: Changing the degrees of freedom on the fly. *J. Chem. Phys.* **2005**, *123*, 224106.
(142) Jeffery, G. B. The motion of ellipsoidal particles immersed in a viscous fluid. In *Proceedings of the Royal Society of London. Series A, Containing papers of a mathematical and physical character*, 1922, pp 161−179.
(143) Svetina, S.; Ottova-Leitmannová, A.; Glaser, R. Membrane bending energy in relation to bilayer couples concept of red blood cell shape transformations. *J. Theor. Biol.* **1982**, *94*, 13−23.
(144) Svetina, S.; Žekš, B. Bilayer couple hypothesis of red cell shape transformations and osmotic hemolysis. *Biomed. Biochim. Acta* **1983**, *42*, S86.
(145) Svetina, S.; Žekš, B. Membrane bending energy and shape determination of phospholipid vesicles and red blood cells. *Eur. Biophys. J.* **1989**, *17*, 101−111.
(146) Svetina, S.; Žekš, B.; Waugh, R.; Raphael, R. Theoretical analysis of the effect of the transbilayer movement of phospholipid molecules on the dynamic behavior of a microtube pulled out of an aspirated vesicle. *Eur. Biophys. J.* **1998**, *27*, 197−209.
(147) Heinrich, V.; Božič, B.; Svetina, S.; Žekš, B. Vesicle deformation by an axial load: from elongated shapes to tethered vesicles. *Biophys. J.* **1999**, *76*, 2056−2071.
(148) Derganc, J.; Božič, B.; Svetina, S.; Žekš, B. Equilibrium shapes of erythrocytes in rouleau formation. *Biophys. J.* **2003**, *84*, 1486−1492.
(149) Ziherl, P.; Svetina, S. Membrane elasticity molds aggregates of simple cells. *Soft Matter* **2008**, *4*, 1937−1942.
(150) Bian, X.; Litvinov, S.; Koumoutsakos, P. Bending models of lipid bilayer membranes: Spontaneous curvature and area-difference elasticity. *Comput. Meth. Appl. Mech. Eng.* **2020**, *359*, 112758.
(151) Šiber, A.; Božič, A. L.; Podgornik, R. Energies and pressures in viruses: contribution of nonspecific electrostatic interactions. *Phys. Chem. Chem. Phys.* **2012**, *14*, 3746−3765.
(152) Zandi, R.; Dragnea, B.; Travesset, A.; Podgornik, R. On virus growth and form. *Phys. Rep.* **2020**, *847*, 1−102.
(153) Asano, Y.; Watanabe, H.; Noguchi, H. Molecular dynamics simulation of soundwave propagation in a simple fluid. *J. Chem. Phys.* **2020**, *153*, 124504.
(154) Asano, Y.; Watanabe, H.; Noguchi, H. Effects of vapor-liquid phase transitions on sound-wave propagation: A molecular dynamics study. *Phys. Rev. Fluids* **2022**, *7*, 064302.

https://doi.org/10.1021/acsanm.5c02783
ACS Appl. Nano Mater. 2025, 8, 16053−16070